Title

Connecting massive galaxies to dark matter haloes in BOSS – I. Is galaxy colour a stochastic process in high-mass haloes?

Journal

Monthly Notices of the Royal Astronomical Society, 460(2)

ISSN

0035-8711

Authors

Saito, Shun
Leauthaud, Alexie
Hearin, Andrew P
et al.

Publication Date

2016-08-01

DOI

10.1093/mnras/stw1080

Peer reviewed

Monthly Notices
of the
ROYAL ASTRONOMICAL SOCIETY

MNRAS **460,** 1457–1475 (2016)
Advance Access publication 2016 May 6

doi:10.1093/mnras/stw1080

Connecting massive galaxies to dark matter haloes in BOSS – I. Is galaxy colour a stochastic process in high-mass haloes?

Shun Saito,[1⋆] Alexie Leauthaud,[1] Andrew P. Hearin,[2] Kevin Bundy,[1] Andrew R. Zentner,[3] Peter S. Behroozi,[4†] Beth A. Reid,[5†] Manodeep Sinha,[6] Jean Coupon,[7] Jeremy L. Tinker,[8] Martin White[5,9,10] and Donald P. Schneider[11,12]

[1]*Kavli Institute for the Physics and Mathematics of the Universe (WPI), The University of Tokyo Institutes for Advanced Study, The University of Tokyo, Chiba 277-8582, Japan*
[2]*Yale Center for Astronomy and Astrophysics, Yale University, New Haven, CT 06511, USA*
[3]*Department of Physics and Astronomy and Pittsburgh Particle physics, Astrophysics and Cosmology Center (PITT PACC), University of Pittsburgh, Pittsburgh, PA 15260, USA*
[4]*Space Telescope Science Institute, Baltimore, MD21218, USA*
[5]*Lawrence Berkeley National Laboratory, 1 Cyclotron Road, Berkeley, CA 94720, USA*
[6]*Department of Physics and Astronomy, Vanderbilt University, Nashville, TN 37235, USA*
[7]*Astronomical Observatory of the University of Geneva, ch. d'Ecogia 16, CH-1290 Versoix, Switzerland*
[8]*Center for Cosmology and Particle Physics, Department of Physics, New York University, New York, NY 10003, USA*
[9]*Department of Physics, 366 LeConte Hall, University of California at Berkeley, Berkeley, CA 94720, USA*
[10]*Department of Astronomy, 601 Campbell Hall, University of California at Berkeley, Berkeley, CA 94720, USA*
[11]*Department of Astronomy and Astrophysics, The Pennsylvania State University, University Park, PA 16802, USA*
[12]*Institute for Gravitation and the Cosmos, The Pennsylvania State University, University Park, PA 16802, USA*

Accepted 2016 May 4. Received 2016 April 29; in original form 2016 January 24

ABSTRACT

We use subhalo abundance matching (SHAM) to model the stellar mass function (SMF) and clustering of the Baryon Oscillation Spectroscopic Survey (BOSS) 'CMASS' sample at $z \sim 0.5$. We introduce a novel method which accounts for the stellar mass incompleteness of CMASS as a function of redshift, and produce CMASS mock catalogues which include selection effects, reproduce the overall SMF, the projected two-point correlation function $w_{\rm p}$, the CMASS $\mathrm{d}n/\mathrm{d}z$, and are made publicly available. We study the effects of assembly bias above collapse mass in the context of 'age matching' and show that these effects are markedly different compared to the ones explored by Hearin et al. at lower stellar masses. We construct two models, one in which galaxy colour is stochastic ('AbM' model) as well as a model which contains assembly bias effects ('AgM' model). By confronting the redshift dependent clustering of CMASS with the predictions from our model, we argue that that galaxy colours are not a stochastic process in high-mass haloes. Our results suggest that the colours of galaxies in high-mass haloes are determined by other halo properties besides halo peak velocity and that assembly bias effects play an important role in determining the clustering properties of this sample.

Key words: galaxies: haloes – large-scale structure of Universe.

1 INTRODUCTION

The overall picture that galaxies form, evolve, and reside in dark matter haloes that assemble hierarchically has gained consensus by passing a variety of observational tests over a wide range of cosmic history (for a review, see Mo, van den Bosch & White 2010). However, understanding the detailed relation between galaxies and dark matter haloes is critical in order to form a more concrete theory of galaxy formation and evolution. In particular, unveiling how the stellar masses and star formation properties of galaxies depend on halo properties is still a topic of active investigation. For low-mass galaxies ($M_* \lesssim 10^{11}\,\mathrm{M}_\odot$), recent studies of galaxy clustering and galaxy–galaxy lensing suggest that red and blue galaxies live in haloes of different mass at fixed stellar mass at $0 \lesssim z \lesssim 1$ (Zehavi et al. 2005; Mandelbaum et al. 2006; Tinker et al. 2013; Coupon

⋆E-mail: shun.saito@ipmu.jp
† Hubble Fellow.

et al. 2015; Mandelbaum et al. 2016) or that at fixed stellar mass, galaxy colour may correlate with halo age (Hearin et al. 2014).

While many previous studies focus on low- or intermediate-mass galaxies, the galaxy-halo mass connection is also worth investigating for the most massive galaxies in the universe. The majority of galaxies with masses $M_* \gtrsim 10^{11}\,\mathrm{M}_\odot$ are centrals hosted by massive haloes ($M_{\rm halo} \gtrsim 10^{13}\,\mathrm{M}_\odot$) (Leauthaud et al. 2011; White et al. 2011; Coupon et al. 2015). From a theoretical standpoint, gas in these high-mass haloes is thought to be heated by pressure-supported shocks (the so-called hot halo mode, Dekel & Birnboim 2006). In addition, at these halo masses, 'maintenance mode' feedback mechanisms such as radio-mode feedback are thought to further limit star formation in the most massive galaxies (e.g. Croton et al. 2006). Observationally, however, not all massive galaxies are systematically 'red and dead'. For example, although they are rare, brightest cluster galaxies associated with cool core clusters can exhibit star formation rates of order $\mathcal{O}$(10–100) $\mathrm{M}_\odot\,\mathrm{yr}^{-1}$ (e.g. in Abell 1835 at $z \sim 0.25$ and in Perseus A and Cygnus A at $z \sim 0.1$) (e.g. Liu, Mao & Meng 2012; McDonald et al. 2012; Fraser-McKelvie, Brown & Pimbblet 2014). At group scales, Tinker et al. (2012) found that as many as 20 per cent of central galaxies in haloes with $\log_{10}(M_{\rm halo}/\mathrm{M}_\odot) > 13$ at $z \sim 0.5$ have sufficient levels of star formation to exhibit blue colours. A key question is then: what determines colour in high-mass haloes? Is star formation in massive galaxies simply a stochastic process due to episodic amount of gas cooling and/or due to mergers with gas rich satellites? Or are the colours of massive galaxies more fundamentally linked to assembly history of their parent dark matter haloes?

Large spectroscopic samples of massive galaxies are of tremendous value in addressing these types of questions. Spectroscopic redshifts are crucial for computing precise measurements of galaxy-clustering and galaxy–galaxy lensing which can be used to constrain the galaxy-halo connection (e.g. Mandelbaum et al. 2006; Leauthaud et al. 2011; Coupon et al. 2015). The availability of spectroscopic redshifts also reduces uncertainties on stellar mass estimates. Spectroscopic surveys such as zCOSMOS (Lilly et al. 2007), VVDS (Fèvre et al. 2015), DEEP2 (Newman et al. 2013), PRIMUS (Coil et al. 2011), and VIPERS (Guzzo et al. 2014), however, cover relatively small areas ranging from a few square degrees to a few tens of square degrees and do not provide statistically significant samples of the most massive galaxies ($\log_{10}(M_*/\mathrm{M}_\odot) > 11.5$). For this reason, we turn our attention instead to the Sloan Digital Sky Survey III (SDSS-III; Eisenstein et al. 2011) Baryon Oscillation Spectroscopic Survey (BOSS; Dawson et al. 2013). The main BOSS cosmological sample, the so-called *CMASS* sample (Reid et al. 2016), includes roughly half a million massive galaxies at $\log_{10}(M_*/\mathrm{M}_\odot) \gtrsim 11.0$ at $0.43 < z < 0.70$ and covers a gigantic volume of approximately 2.5 $(h^{-1}\,\mathrm{Gpc})^3$ at the 10th data release (DR10) (Ahn et al. 2014). This gigantic data set enables high signal-to-noise ratio measurements of three-dimensional galaxy clustering on large scales (typically separation of $r \gtrsim 10$ Mpc) and provides the most accurate measurement of the Baryon Acoustic Oscillation (BAO) scale and the Redshift-Space Distortion (RSD) signal with a precision in DR11 (Alam et al. 2015) of ≈1 per cent and ≈10 per cent, respectively (e.g. Anderson et al. 2014; Beutler et al. 2014a,b; Samushia et al. 2014).

The main goal of this paper is to model the connection between galaxy mass, colour, and halo mass for massive galaxies using the BOSS CMASS data set. In addition to providing insight on the evolution of massive galaxies, a detailed understanding of the CMASS-halo connection is also critical because BOSS analysis pipelines need to be systematically tested against *realistic* CMASS mock catalogues. Mock catalogues within the BOSS collaboration (e.g. White et al. 2011; Manera et al. 2012; Kitaura, Yepes & Prada 2013; White, Tinker & McBride 2013) are typically based on the Halo Occupation Distribution (HOD) approach (see e.g. Berlind & Weinberg 2002; Zheng et al. 2005). However, until present, most studies have assumed that CMASS is a homogeneous sample and have ignored any redshift-dependent selection effects.

Indeed, one difficulty with the CMASS sample that affects both studies of massive galaxies as well as the creation of realistic mock catalogues, is accounting for the selection function of the sample. The CMASS selection algorithm was roughly designed to select a '*constant stellar-mass*' sample and is often quoted as being mass limited at $\log_{10}(M_*/\mathrm{M}_\odot) > 11.3$ over the redshift range $0.43 < z < 0.7$. However, Leauthaud et al. (2016, hereafter L16) demonstrate that CMASS is only 80 per cent complete at $\log_{10}(M_*/\mathrm{M}_\odot) > 11.6$ in the narrow redshift range $0.51 < z < 0.61$. Our paper improves on previous analyses by presenting a careful treatment of the stellar mass completeness of the CMASS sample in our models.

To model the CMASS-halo connection we adopt the subhalo abundance matching (SHAM) technique. SHAM is a fairly simple and empirical approach which assumes that galaxy properties such as luminosity or stellar mass are monotonically related to (sub)halo properties such as mass or circular velocity (see e.g. Kravtsov et al. 2004; Vale & Ostriker 2004; Conroy, Wechsler & Kravtsov 2006; Behroozi, Conroy & Wechsler 2010; Moster et al. 2010). Although there are model ambiguities in this method (e.g. in choosing which properties to relate and how scatter is introduced), SHAM requires relatively few parameters and also provides a straightforward prescription for linking galaxy properties to dark matter haloes in numerical *N*-body simulations. Our work can be considered as an update to Nuza et al. (2013) who used the SHAM approach to model the CMASS-halo connection but without accounting for the stellar mass completeness of the CMASS sample.

In addition to the standard implementation of SHAM, we also explore the *age matching* model introduced by Hearin et al. (2013, hereafter H13) which introduces galaxy colour by assuming that at fixed stellar mass, redder galaxies reside in older sub-haloes. The age matching scheme can qualitatively explain a variety of observed statistics in the SDSS main galaxy sample including colour-dependent galaxy clustering (H13; Watson et al. 2014), magnitude gap statistics in galaxy groups (Hearin et al. 2013), galaxy–galaxy lensing (Hearin et al. 2014), galaxy conformity (Hearin, Watson & van den Bosch 2015), and halo mass dependence of the specific star formation rate (Lim et al. 2016).

Our models are constrained by three observables: the clustering of CMASS on radial scales $r \lesssim 0.1$–10 Mpc, the galaxy stellar mass function (SMF), and the SMF of CMASS galaxies as a function of redshift.

This paper is organized as follows. The observational data are summarized in Section 2. Our measurements of the correlation function and the galaxy SMF are described in Section 3. In particular, Section 3.3 presents our measurements of the redshift-dependent CMASS SMFs that are an essential ingredient in this study. Section 4 briefly summarizes the simulated subhalo catalogue. Section 5 is a detailed presentation of our SHAM and age matching methodology. Our results are described in Section 6 and discussed in Section 7. Finally we summarize and conclude our study in Section 8.

Our measurements assume a flat ΛCDM cosmology with $\Omega_{\rm m} = 0.274$ and $H_0 = 70\,\mathrm{km\,s^{-1}\,Mpc^{-1}}$. For all quantities related to $w_{\rm p}$, or to *N*-body simulations, we adopt $H_0 = 100\,h\,\mathrm{km\,s^{-1}\,Mpc^{-1}}$ and hence distance and mass units are written as h^{-1} Mpc and $h^{-1}\,\mathrm{M}_\odot$.

Note that there are small differences between this choice and the cosmological parameters assumed for the *N*-body simulations that we introduce in Section 4.

2 OBSERVATIONAL DATA

This section begins with a brief review of the BOSS DR10 CMASS sample. In addition to the BOSS sample, our analysis also relies on data from the SDSS Stripe 82 region which is roughly two magnitudes deeper than the SDSS main survey.

2.1 The BOSS DR10 CMASS sample

The BOSS survey (Dawson et al. 2013) is a part of SDSS-III which measured 1.5 million spectroscopic redshifts of luminous galaxies and 160 000 quasars over an extragalactic footprint covering $\sim$10 000 deg^2. Spectroscopic observations were obtained using the 1000 object fibre-fed BOSS spectrograph (Smee et al. 2013) on the 2.5 m aperture Sloan Foundation Telescope at the Apache Point Observatory (Gunn et al. 1998, 2006). The BOSS pipeline is described in Bolton et al. (2012), and BOSS galaxies were selected from Data Release 8 (DR8; Aihara et al. 2011) *ugriz* photometry (Fukugita et al. 1996). The main purpose of BOSS is to measure the BAO feature and RSD from galaxy clustering. The internal data release 11 (DR11) and the final DR12 data set are made public in Alam et al. (2015), although the DR12 large-scale structure CMASS catalogue is not yet publicly available at this point. Using DR11 which contains nearly one million spectroscopic redshifts of galaxies over $\sim$8500 deg^2, the BOSS collaboration has measured BAO and RSD signals to an unprecedented precision of 1 per cent and 10 per cent, respectively (e.g. Anderson et al. 2014; Beutler et al. 2014a,b; Samushia et al. 2014)

The BOSS target selection is divided into two samples, a low-redshift sample ('LOWZ') that selects luminous red galaxies at $z < 0.43$ (for details see Tojeiro et al. 2014) and a high-redshift sample ('CMASS') that targets galaxies at $0.43 < z < 0.7$ (Reid et al. 2016). This paper focuses only on the CMASS sample which is selected using a series of colour–magnitude cuts motivated by stellar population models from Maraston et al. (2009). The CMASS sample is selected as:

$$17.5 < i_{\rm cmod} < 19.9,$$

$$r_{\rm mod} - i_{\rm mod} < 2.0,$$

$$d_\perp > 0.55,$$

$$i_{\rm fib2} < 21.5,$$

$$i_{\rm cmod} < 19.86 + 1.6(d_\perp - 0.8), \quad (1)$$

where

$$d_\perp = r_{\rm mod} - i_{\rm mod} - (g_{\rm mod} - r_{\rm mod})/8.0. \quad (2)$$

Model magnitudes are denoted with the subscript 'mod', composite model magnitudes are denoted with the subscript 'cmod', fibre magnitude within a 2 arcsec aperture is denoted with the subscript 'fib2'. The BOSS colour cuts are computed using model magnitudes, whereas magnitude cuts are computed using cmodel magnitudes. All magnitudes are corrected for Galactic extinction using the dust maps of Schlegel, Finkbeiner & Davis (1998).

In this paper, we use the CMASS sample from the public DR10 data set (Ahn et al. 2014) that includes 409 365 galaxies over 4892 deg^2 in the North Galactic Cap (NGC) and 112 593 galaxies over 1432 deg^2 in the South Galactic Cap (SGC). Note that these numbers differ from those reported in Anderson et al. (2014) simply because we adopt a different weighting scheme for our clustering measurements (see following section). While previous studies have focused on sub-samples of CMASS in limited redshift or magnitude ranges (e.g. Guo et al. 2013, 2014; Miyatake et al. 2015; More et al. 2015), in this paper we model the full CMASS sample over the full redshift range $0.43 < z < 0.7$.

2.2 Stripe 82 Co-add catalogue combined with UKIDDS photometry for improved stellar mass estimates

A key aspect of our approach is the use of Stripe 82 – a deeper but narrower subset of the survey area – for which it is possible to construct a galaxy sample with a well-understood completeness function. Stripe 82 provides two key advantages. First, it was the subject of repeat imaging campaigns in SDSS and therefore reaches *ugriz* depths that are roughly two magnitudes deeper than the single-epoch SDSS imaging that was used to construct the BOSS target catalogue. This added depth is critical for obtaining reliable photometric redshifts (photo-z's) for massive galaxies ($\log_{10}(M_*/{\rm M}_\odot) > 11$) that can be used to supplement the colour-selected BOSS samples out to $z \sim 0.7$. Secondly, Stripe 82 was imaged by the UKIRT Infrared Deep Sky Survey (UKIDSS, Lawrence et al. 2007) providing near-IR photometry for robust stellar mass estimates.

In this paper, we use the Stripe 82 Massive Galaxy catalogue (hereafter, s82-MGC). The s82-MGC catalogue construction, photometric matching, redshift validation, masking, and other details are described in Bundy et al. (2015). The s82-MGC catalogue contains all classified galaxies from UKIDSS-LAS frames with 10σ detection limits deeper than $YJHK = [20.2, 20.2, 20.2, 20.6]$ (AB) (Oke & Gunn 1983). These limits are those roughly needed for 10σ detections in these bands of $z \sim 0.6$ passive galaxies with $\log_{10}(M_*/{\rm M}_\odot) > 11.2$. UKIDSS and BOSS masks are applied to this catalogue which covers a total area of 139.4 deg^2.

The s82-MGC catalogue contains both spectroscopic and photometric redshifts. For each galaxy, we adopt the spectroscopic redshift when it is available and use the photometric redshift otherwise. L16 demonstrate that the impact of photo-z scatter on the high-mass end of the SMF is negligible. Stellar masses are estimated for this catalogue by applying the SED-fitting code described in Bundy et al. (2010) to the SDSS+UKIDSS PSF-matched photometry. For a prior grid of SED templates and a Chabrier IMF (Chabrier 2003), an M_* probability distribution is obtained by scaling the model M/L ratios by the inferred luminosity in the observed K-band, or H-band if a K-band magnitude is not available. The median of this distribution is taken as the M_* estimate.

3 CORRELATION FUNCTION AND SMF MEASUREMENTS

This section summarizes our measurements of several statistics derived from the observational data described in the previous section. After briefly explaining the measurement of the two-point correlation function (note that we use the measurement computed by Reid et al. (2014, hereafter R14)), we present our measurement of the CMASS SMFs as a function of redshift.

3.1 The CMASS two-point correlation function

In this paper we adopt the DR10 projected two-point correlation function, w_p, and the monopole and quadrupole of the correlation

function, $\hat{\xi}_\ell$, and the associated covariance matrices determined by R14. We only give a brief summary of how these measurements were performed; we refer the reader to R14 for additional details. The two-dimensional redshift-space correlation function $\xi(\boldsymbol{s})$ is measured using the Landy–Szalay estimator Landy & Szalay (1993):

$$\xi(\boldsymbol{s}) = \frac{\mathrm{DD}(\Delta\boldsymbol{s}) - 2\mathrm{DR}(\Delta\boldsymbol{s}) + \mathrm{RR}(\Delta\boldsymbol{s})}{\mathrm{RR}(\Delta\boldsymbol{s})}, \quad (3)$$

where DD, DR, and RR are the data–data, data–random, and random–random pairs in a given bin $[\boldsymbol{s} - \Delta\boldsymbol{s}/2, \boldsymbol{s} + \Delta\boldsymbol{s}/2]$. The randoms account for the survey geometry and for the completeness factor which depends on angular position and a radial selection function, $\mathrm{d}n/\mathrm{d}z$. The correlation function is integrated over the line-of-sight separation to obtain the projected correlation function (Davis & Peebles 1983),

$$w_p(r_p) = 2\int_0^{r_{\pi,\max}} \xi(r_p, r_\pi)\,\mathrm{d}r_\pi, \quad (4)$$

where the three-dimensional pair separation $\boldsymbol{s}$ in redshift space is split into a component transverse (r_p) and parallel (r_π) to the line-of-sight direction. The integral is performed to $r_{\pi,\max} = 80\,h^{-1}$ Mpc and w_p is measured from 0.194 h^{-1} Mpc to 25.98 h^{-1} Mpc with 18 equally spaced logarithmic bins. The advantage of using the projected correlation function is that it is less sensitive than $\xi(\boldsymbol{s})$ to the effects of galaxy peculiar velocities. Note that, however, we do account for the RSD effect (van den Bosch et al. 2013) in our modelling through the velocity of subhaloes. The projected two-point correlation function is measured separately for the North and South Galactic Caps and these measurements are combined using a simple average, weighted by the number of CMASS galaxies in each hemisphere.

The w_p measurement from R14 does not use the optimal weights (the so-called FKP weights), or the systematic weights (Anderson et al. 2014). The systematic weights affect large scales and hence are not relevant for our small-scale measurement. Also, this approach enables a fairer comparison with our measurement of the galaxy SMF which does not use any weighting schemes. Weights are applied, however, to account for redshift failures and for fibre collisions. Fibre collisions are particularly important for small scale clustering measurements with BOSS – the fibre-collision scale in BOSS is 62 arcsec which corresponds to a comoving scale of $\sim$0.45 h^{-1} Mpc at $z \sim 0.57$. To complicate matters, the BOSS tiling strategy also introduces a correlation between fibre collisions and the density field. R14 studied the impact of fibre collisions for the CMASS sample using tiled mock catalogues. They adopt a radial dependent correction scheme in which an angular up-weighting method is used at $r_p < 1.09\,h^{-1}$ Mpc and a nearest neighbour (NN) weighting scheme is used at larger scales. Finally, the correlation function is debiased for residual fibre-collision effects using the tiled mock catalogues.

The covariance matrix for w_p, $\boldsymbol{C}_{w_\mathrm{p},\mathrm{boot}}$, is derived from 5000 000 realizations drawn from 200 bootstrap regions which are roughly equal in size and shape. An additional 10 per cent uncertainty due to the angular up-weighting method and the debiasing procedure are propagated into the diagonal element of the covariance matrix. As a result, the measurement error on w_p increases below $r_p = 1.09\,h^{-1}$ Mpc. Finally, the inverse covariance matrix is corrected following Hartlap, Simon & Schneider (2007). With $n_\mathrm{boot} = 200$ and $n_\mathrm{bin} = 18$, this leads to a 0.904 correction to the final inverse covariance matrix, $\boldsymbol{C}^{-1}_{w_\mathrm{p},\mathrm{meas}} = 0.904\boldsymbol{C}^{-1}_{w_\mathrm{p},\mathrm{boot}}$.

In addition to w_p, we will also use the monopole and quadrupole of the correlation function which contain information about the peculiar velocities of galaxies. Again, following R14, we adopt the pseudo multipole correlation function defined by

$$\hat{\xi}_\ell(s) = (2\ell+1)\int_0^{\mu_\mathrm{max}(s)} \mathrm{d}\mu\,\xi(s,\mu)\mathcal{L}_\ell(\mu), \quad (5)$$

where $s^2 = r_\mathrm{p}^2 + r_\pi^2$, $\mu = r_\pi/s$, and $\mathcal{L}_\ell(\mu)$ is the ℓth order Legendre polynomial. The integration over the azimuthal angle μ is performed up to $\mu_\mathrm{max}(s) \equiv 0.534\,\mathrm{s}^{-1}$ in order to minimize the impact of fibre collisions on the small-scale measurements. We refer the reader to R14 for further details.

3.2 The Stripe 82 SMF at $z = 0.55$

As shown in L16, the CMASS sample is only stellar mass complete at the high-mass end and in a narrow redshift range. To perform abundance matching, however, we need to measure the total SMF. Indeed, for abundance matching, a complete galaxy sample is necessary when rank ordering galaxies versus haloes.

Bundy et al. (2015) present an estimate of the SMF at $z \sim 0.5$ by using the s82-MGC catalogue. In order to compute the SMF, Bundy et al. (2015) use a combination of spectroscopic redshifts, supplemented with photometric redshifts (photo-zs) when a spectroscopic redshift is not available. We adopt a similar approach and compute the SMF from the s82-MGC at $\log_{10}(M_*/\mathrm{M}_\odot) > 10.5$ over $0.43 < z < 0.70$. Our analysis assumes that the SMF does not vary over this redshift range. The result is shown in Fig. 1. Error bars on the SMF represent the square root of the diagonal component of the covariance matrix, which is estimated from the data using 214 nearly equal area bootstrap regions.

Because the majority of galaxies at the high-mass end have a spectroscopic redshift, the impact of photo-z uncertainty on the Stripe 82 SMF is negligible (see L16), i.e. the use of photometric redshifts only adds a negligible amount of scatter in the total stellar mass estimate and does not inflate the high-mass end of the SMF.

The left-hand panel of Fig. 1 presents a comparison between our SMF with results from COSMOS (Leauthaud et al. 2011) and PRIMUS (Moustakas et al. 2013) at similar redshifts. Fig. 1 demonstrates that, because of the large area covered by Stripe 82, the high-mass end of the total SMF is tightly constrained at $\log_{10}(M_*/\mathrm{M}_\odot) > 11.3$ over $0.43 < z < 0.70$, while COSMOS and PRIMUS constrain the low-mass end. The comparison with COSMOS and PRIMUS suggests that the s82-MGC is complete to $\log_{10}(M_*/\mathrm{M}_\odot) \sim 11.2$ at $z = 0.7$ (Bundy et al. 2015).

We will use the s82-MGC SMF measured using eight data points over the range $11.5 \leq \log_{10}(M_*/\mathrm{M}_\odot) \leq 12.0$. The inverse covariance matrix for the s82-MGC SMF, $\boldsymbol{C}^{-1}_\mathrm{SMF}$ is computed as follows. First we compute the covariance matrix $\boldsymbol{C}_\mathrm{SMF,boot}$ from 214 bootstrap regions, and then smooth the noise in the non-diagonal components using a boxcar algorithm (Mandelbaum et al. 2006). Finally we multiply by the Hartlap correction factor which is $\sim$0.958, i.e. $\boldsymbol{C}^{-1}_\mathrm{SMF} = 0.958\boldsymbol{C}^{-1}_\mathrm{SMF,boot}$. Although the error budget is dominated by the Poisson noise which only contributes to diagonal components (Smith 2012), the Poisson error underestimate the errors. We find that the diagonal component in our jackknife covariance matrix is larger than the Poisson errors by a factor of $\sim$30 per cent in the mass range of our interest.

3.3 SMF of CMASS galaxies as a function of redshift

The other ingredient that will be important in our analysis are the SMFs of CMASS galaxies as a function of redshift. The right-hand panel of Fig. 1 shows SMFs for CMASS galaxies measured using

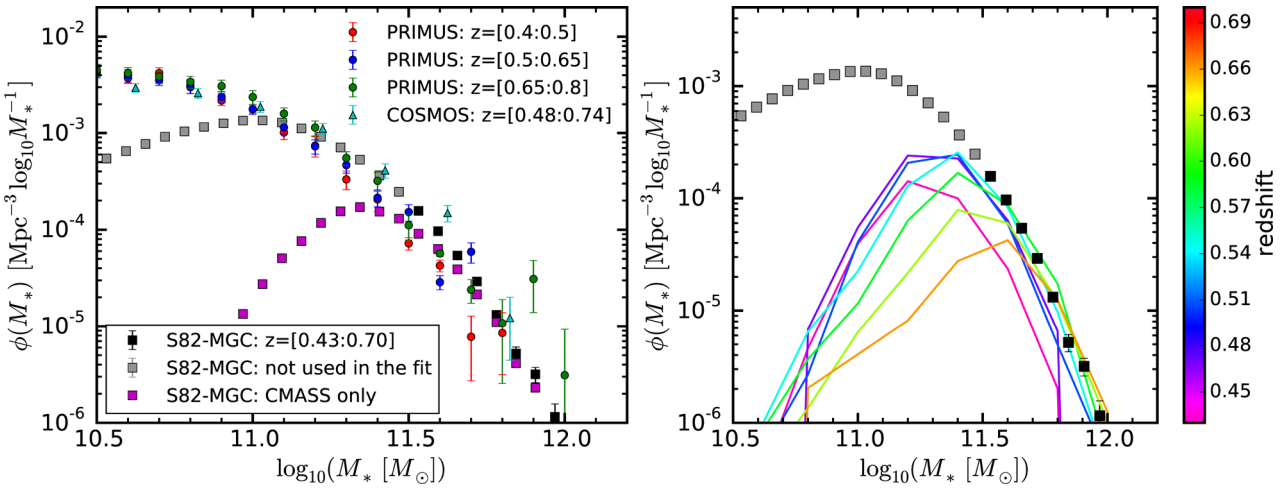

Figure 1. (Left) The total SMF from Stripe 82 (black and grey squares) measured from s82-MGC (139.4 deg^2) and the SMF measured using only CMASS galaxies (magenta squares). Other SMFs determined from smaller area surveys at similar redshifts are also shown. Red, blue, and green circles indicate results from PRIMUS (5.5 deg^2) at $0.4 < z < 0.5$, $0.5 < z < 0.65$, and $0.65 < z < 0.8$, respectively. Cyan triangles represent one wide redshift bin from the COSMOS survey (1.64 deg^2). As explained later, we only use data points with $\log_{10}(M_*/\mathrm{M}_\odot) > 11.5$ (black squares) when fitting against the SMF data. (Right) SMFs as a function of redshift measured using only the CMASS sample. As a reference, we also present the total SMF from the s82-MGC at $0.43 < z < 0.70$ and $\log_{10}(M_*/\mathrm{M}_\odot) > 10.5$. As demonstrated in L16, the CMASS SMFs vary with redshift and CMASS is only complete in terms of stellar mass at the highest masses and in a relatively narrow redshift range.

the s82-MGC in seven redshift bins with $\Delta z = 0.04$. As can be seen from the right-hand panel of Fig. 1, the completeness of CMASS depends both on redshift and stellar mass; this is because the effects of the magnitude and colour cuts that define the CMASS sample vary with redshift. The utility of the these CMASS SMFs will be apparent when we describe our methodology in Section 5.

4 SUBHALO CATALOGUE

In this section we present the *N*-body simulation and subhalo catalogue that is an essential ingredient in our abundance-matching study. We also perform tests of the completeness of the subhalo catalogue.

4.1 *N*-body simulation

Because the BOSS DR10 CMASS sample covers a large comoving volume, $V \sim 2.6\,(h^{-1}\,\mathrm{Gpc})^3$, with a high number density of $\overline{n} \sim 3 \times 10^{-4}\,(h^{-1}\,\mathrm{Mpc})^{-3}$, our analysis requires a large volume *N*-body simulation that can resolve haloes to 10^{12} $\mathrm{M}_\odot$. We use the publicly available MultiDark simulation, MDR1 (Prada et al. 2012; Riebe et al. 2013). The cosmological parameters in MDR1 are consistent with a flat *WMAP*5 ΛCDM cosmology (Komatsu et al. 2009): $\Omega_{\mathrm{m0}} = 0.27$, $\Omega_\Lambda = 0.73$, $\Omega_{\mathrm{b0}} = 0.047$, $n_\mathrm{s} = 0.95$, and $\sigma_8 = 0.82$. This cosmology is similar to the one used for our measurements of the clustering signals, therefore safely ignore the cosmological uncertainty in the distance scale (More 2013). MDR1 is a $L_{\mathrm{box}} = 1.0\,h^{-1}$ Gpc simulation with a particle mass of $8.7 \times 10^9\,h^{-1}\,\mathrm{M}_\odot$ ($N_{\mathrm{par}} = 2048^3$ particles). We use an output at $z = 0.534$ which is close to the peak of the BOSS CMASS dn/dz at $z \sim 0.55$.

4.2 Halo catalogues and merger trees

Haloes and subhaloes are identified using the Rockstar algorithm (Behroozi et al. 2013b; Behroozi, Wechsler & Wu 2013a). Rockstar is a phase-space halo finder that also considers halo merger histories to provide a robust and stable identification of haloes and subhaloes. The advantages of Rockstar compared to other halo finders are well documented in Knebe et al. (2011) and Onions et al. (2012). These studies suggest that among halo finders, Rockstar finder is the least sensitive to resolution effects. Rockstar, with the Consistent Trees algorithm, produces halo merger trees and catalogues with various parameters derived from the halo assembly history, including, for example, V_{peak}, the maximum halo circular velocity for each subhalo.

We use the '*Z*'-axis of the MDR1 simulation as the line-of-sight direction. In order to maximize the volume of our mock, we re-map the 1-h^{-1}Gpc MDR1 cube into a cuboid of dimensions, $(X, Y, Z) = (3.7417, 0.4082, 0.6547)L_{\mathrm{box}}$ following the method developed by Carlson & White (2010). After remapping, the *Z*-axis has a length of $654.7\,h^{-1}$ Mpc corresponding to a redshift range of $0.42 < z < 0.71$. This includes a margin that is sufficient to account for peculiar velocities at the boundary of our mock catalogue.

Peculiar velocities of subhaloes are defined as the average velocity of particles within the innermost 10 per cent of the virial radius. The virial overdensity in Rockstar is defined by $\Delta_{\mathrm{vir}} \approx 237\rho_{\mathrm{m}}$ at $z = 0.534$. This definition does *not* correspond to the definition of the halo bulk flow velocity that uses all particle members of the halo, because the halo core and its outer regions have different velocity structure. For a demonstration of this point, see fig. 11 of Behroozi et al. (2013b) and also appendix B of R14.[1] All subhaloes are mapped into redshift space by including the peculiar velocity component along the *Z* direction before performing abundance matching.

4.3 Time evolution and resolution tests

In this section, we discuss potential issues in the subhalo catalogue, focusing in particular on the time evolution of subhalo clustering and completeness issues due to the resolution of the simulation.

[1] The definition of halo peculiar velocity in R14 is the average of particles within ∼33 per cent of the virial radius where $\Delta_{\mathrm{vir}} \approx 200\rho_{\mathrm{m}}$.

Here we only summarize our findings – figures and further details can be found in Appendix A.

We adopt a single redshift output at $z = 0.534$ from the MDR1 simulation. We test if a single redshift output is sufficient to model CMASS over the redshift range $0.43 < z < 0.7$. There are three outputs available in the MDR1 simulation over the redshift range of interest: $z = 0.466$, 0.534 and 0.609. Using these redshift outputs, we find a difference in the real-space correlation function at fixed number density, $\bar{n} \simeq 1.58 \times 10^{-4} (h^{-1}\,\mathrm{Mpc})^{-3}$, at the 1–2 per cent level at large scales. The largest differences (at the level of 5 per cent) are seen at the 1-halo to 2-halo regime at $r \lesssim 1\,h^{-1}$ Mpc (see Appendix A). This level of evolution is below our measurement errors, but these effects will need to be taken into account in future work, especially when the S/N of the measurements increases (currently we are using DR10 measurements).

We also perform two tests concerning the impact of the resolution of MDR1 on our results. First, we determine if the subhalo catalogue resolves the mass scale required for our abundance matching. Based on White et al. (2011) and R14, we estimate that abundance matching for CMASS will require subhaloes with $V_{\rm peak} \geq 200\,\mathrm{km\,s^{-1}}$. Our tests demonstrate that MDR1 resolves haloes down to $V_{\rm peak} \sim 150\,\mathrm{km\,s^{-1}}$.

Secondly, we examine the impact of resolution effects on the radial profiles of subhaloes. Our estimates suggest that subhalo radial profiles become incomplete at 0.1–0.7 h^{-1} Mpc (and depend on the ratio between the peak velocity of hosts and subhaloes). The smallest scale in our w_p measurement is $\approx 0.2\,h^{-1}$ Mpc and is close to this incompleteness limit. The impact of resolution on our results is at least partly counteracted by the boost to the errors of our measured w_p by systematic fibre-collision correction uncertainties on these scales. We conclude that the resolution of MDR1 is sufficient for our purpose, but that recently completed higher resolution simulations such as Skillman et al. (2014) or Ishiyama et al. (2015) would be preferable and will be adopted in subsequent work.

5 METHODOLOGY

Our goal is to find a model of the CMASS-halo connection which can simultaneously explain the SMF and the two-point correlation function and which also accounts for stellar mass completeness of CMASS. This section explains the details of our methodology. In this paper we only explore models that reproduce the projected two-point correlation function of the full CMASS sample over the redshift range of $0.43 < z < 0.7$. In future work we will explore how well our models match the clustering of sub-samples (e.g. dividing CMASS by colour and redshift).

We begin with a broad overview of our global methodology and the two classes of models explored in this paper. The details of our approach are then provided in the later half of this section. The casual reader may wish to read the overview of the methodology and then skip directly to the summary provided in Section 5.6.

5.1 Overview of methodology and models

Our approach is based on the SHAM framework for connecting galaxies and dark matter haloes (see Section 5.2). Within the context of SHAM, we will explore two broad classes of models that relate galaxy colour to halo properties. The first model that we explore is a 'stochastic model' in which at fixed stellar mass, galaxy colour in high-mass haloes is simply a random process that does not correlate with halo properties. We will refer to this model as the 'AbM' model. After abundance matching our mock catalogue, we *tag* CMASS galaxies by randomly downsampling the full mock galaxy catalogue in such a way that the mock CMASS SMFs reproduce the ones measured in Section 3.3. Unless an additional correlation between this CMASS flag and halo properties is explicitly introduced, this procedure makes the implicit assumption that *at fixed stellar mass, CMASS galaxies are a random sample of the overall population*. However, L16 show that at fixed stellar mass, CMASS is not a random sample of the overall population in terms of galaxy colour. Hence, the abundance matched catalogue that we obtain after the downsampling procedure will only correctly represent the true relation between galaxy colour, stellar mass, and halo properties if colour is a random process at fixed stellar mass.

The second model is an extension to the traditional abundance matching scheme introduced by H13 called *age matching*. This model is based on the premise that galaxy colour correlates with a secondary halo property at fixed stellar mass (see Section 5.3). After first abundance matching our mock catalogue, the age-matched model will be built by re-shuffling CMASS galaxies according to a secondary halo property. In order to fully implement the age-matching model, however, we need to characterize the colour distributions of galaxies from the S82-MGC as a function of mass and redshift and also to understand the effects of scatter introduced in these colour distributions from photometric redshifts. This is a non-trivial task that we defer to Paper II – opting here instead to simply perform a *qualitative* investigation of the effects of age matching on the two-point correlation function. For this purpose, we will adopt a simple colour model for the galaxy population that is based on a 'colour-rank distribution' represented by $X_{\rm col}$ which effectively characterizes the colour ranking of the CMASS versus other galaxies. This distribution is characterized by one free parameter called $\mu_{\rm CMASS}$. As described in Section 5.3, this parameter controls the correlation strength between subhalo properties and the CMASS selection function.

5.2 Subhalo abundance matching

The SHAM scheme provides an effective and simple way to model the galaxy-halo relation and has been successful at modelling both the galaxy SMF as well as the galaxy two-point correlation function (see e.g. Kravtsov et al. 2004; Vale & Ostriker 2004; Conroy et al. 2006; Behroozi et al. 2010; Moster et al. 2010). The basic philosophy of SHAM is that massive (sub)haloes host bright galaxies. More concretely, the SHAM method begins by rank ordering galaxies by stellar mass M_* (or luminosity). Haloes drawn from N-body simulations are rank ordered by peak maximum circular velocity $V_{\rm peak}$. Galaxies are then assigned to subhaloes in descending order such that $n_{\rm gal}(> M_*) = n_{\rm halo}(> V_{\rm peak})$. In practice, there are multiple ambiguities in the SHAM technique. First, there is freedom in choosing how to rank order subhaloes. For example, Reddick et al. (2013) showed how the predicted two point correlation function varies when rank ordering is performed using different halo mass proxies such as halo mass $M_{\rm vir}$, maximum circular velocity $V_{\rm circ}$, and its peak over entire merging history, $V_{\rm peak}$. Motivated by this work, we will evaluate how our model varies when rank ordering by either $V_{\rm peak}$ or $M_{\rm peak}$. Secondly, SHAM models must also account for scatter between galaxy properties and halo properties. We account for scatter by adopting the methodology of Behroozi et al. (2010) and Reddick et al. (2013).

To perform abundance matching, we need to evaluate the total SMF over the entire mass range covered by the CMASS sample, i.e. down to $\log_{10}(M_*/\mathrm{M}_\odot) \sim 10.6$. This value is below the completeness limit of the S82-MGC. Our strategy will be to fit the total

SMF from the s82-MGC in the range $\log_{10}(M_*/\mathrm{M}_\odot) > 11.5$ using a double Schechter function (Baldry, Glazebrook & Driver 2008):

$$\phi(M_*;\phi_1,\alpha_1,\phi_2,\alpha_2,M_0) = \left\{\phi_1 10^{(\alpha_1+1)(\log M_* - \log M_0)} + \phi_2 10^{(\alpha_2+1)(\log M_* - \log M_0)}\right\} (\ln 10) \exp\left[-\frac{M_*}{M_0}\right], \quad (6)$$

where $|\alpha_2| > |\alpha_1|$ and the second term dominate at the low-mass end. The amplitude of the SMF below $\log_{10}(M_*/\mathrm{M}_\odot) = 11.5$ is unconstrained by the s82-MGC SMF but will be adjusted by our joint fit to the clustering of CMASS galaxies. Section 6 shows that our joint fit to the s82-MGC SMF and to w_p yields an SMF that is consistent at the low-mass end with results from PRIMUS and COSMOS.

We abundance match subhaloes against this SMF, and convolve it with a uniform log-normal scatter,

$$\phi_{\rm conv}(M_*;\phi_1,\alpha_1,\phi_2,\alpha_2,M_0,\sigma) = \int \mathrm{d}m \, \frac{\phi(10^m)}{\sqrt{2\pi}\sigma} \exp\left[-\frac{(m-\log M_*)^2}{2\sigma^2}\right], \quad (7)$$

which introduces a scatter in the relation between stellar and halo mass. This scatter arises due to a combination of intrinsic scatter in the stellar-to-halo-mass relation and errors associated with stellar mass measurements (Behroozi et al. 2010; Leauthaud et al. 2011). Hence, for a realistic model, the value of σ must be equal to, or greater than, the measurement errors in stellar mass measurements – we will return to this question in Section 6.

We fit the s82-MGC SMF over eight data points at $11.5 \leq \log_{10}(M_*/\mathrm{M}_\odot) \leq 12.0$. Our SMF measurements probe the high-mass end of the SMF and hence are insensitive to some parameters in the double Schechter function. For this reason, in our fits, we simply fix the parameters that is not sensitive to the very high-mass end to $(\alpha_1, \phi_2, \alpha_2) = (-0.46, 3.0 \times 10^{-4}, -1.58)$. This is motivated by results at the low-mass end from Baldry et al. (2008). In summary, our abundance matching model contains three free parameters, ϕ_1, M_0, and σ.

We compute a χ^2 for the s82-MGC SMF as follows:

$$\chi^2_{\rm SMF} = \sum_{ij} [\phi_{\rm meas}(M_{*,i}) - \phi_{\rm conv}(M_{*,i};\phi_1,M_0,\sigma)] \times \boldsymbol{C}^{-1}_{{\rm SMF},ij} [\phi_{\rm meas}(M_{*,j}) - \phi_{\rm conv}(M_{*,j};\phi_1,M_0,\sigma)] \quad (8)$$

where $\phi_{\rm conv}(M_*;\phi_1,M_0,\sigma)$ is the theoretical SMF predicted by equation (7).

5.3 Subhalo age matching

SHAM essentially specifies the stellar-to-halo mass relation between galaxies and haloes. It is normally assumed that halo mass is the primary variable on which the galaxy-halo connection depends. However, in addition to halo mass, halo clustering also depends on other parameters such as halo age, a phenomenon known as *assembly bias* (see e.g. Gao, Springel & White 2005; Wechsler et al. 2006; Jing, Suto & Mo 2007; Gao & White 2007; Dalal et al. 2008; Li, Mo & Gao 2008; Lin et al. 2016; Miyatake et al. 2016).

H13 introduced an extension to the traditional abundance matching scheme called *age matching* which can reproduce the colour-dependent clustering of the SDSS main galaxy sample (also see Masaki, Lin & Yoshida 2013). This method matches galaxies and haloes using both stellar mass as well as galaxy colour. The basic premise of the approach is that redder galaxies are assigned to older subhaloes at fixed stellar mass.

In the age matching scheme, each halo is assigned a characteristic redshift ($z_{\rm starve}$) computed from halo merger trees. This $z_{\rm starve}$ parameter is defined as the maximum of three distinct age components.

(i) $z_{\rm char}$: the earliest redshift at which the most massive progenitor of a given subhalo exceeds $M_h > 10^{12}\,h^{-1}\,\mathrm{M}_\odot$. For subhaloes less massive than $10^{12}\,h^{-1}\,\mathrm{M}_\odot$, $z_{\rm char} = z_{\rm obs}$.

(ii) $z_{\rm acc}$: the epoch when a subhalo accretes on to a host halo. For host haloes, $z_{\rm acc} = z_{\rm obs}$.

(iii) $z_{\rm form}$: the epoch defined by $z_{\rm form} = c_{\rm vir}/(4.1 a_{\rm acc}) - 1$, motivated by the fact that there is a tight correlation between the concentration parameter and the epoch when halo growth transits from a fast to slow accretion regime (Wechsler et al. 2006). Note that $a_{\rm acc} = 1/(1 + z_{\rm acc})$.

We adopt $z_{\rm obs} = 0.534$ while in the original work of H13, $z_{\rm obs} = 0$.

There is a critical difference between this work and H13: our relevant mass regime ($\log_{10}(M_*/\mathrm{M}_\odot) \gtrsim 11$) is much higher than that of H13 ($\log_{10}(M_*/\mathrm{M}_\odot) \lesssim 11$). H13 found that $z_{\rm form}$ is the dominant component of $z_{\rm starve}$ for the SDSS main sample whereas we find that $z_{\rm char}$ is the dominant component for CMASS (see Section 6). This is in keeping with the results shown in fig. 5 of Hearin et al. (2014), which demonstrates that $z_{\rm char}$ begins to dominate the contribution to $z_{\rm starve}$ for stellar masses $\log_{10}(M_*/\mathrm{M}_\odot) \gtrsim 11.5$ at $z \sim 0$. In our CMASS sample, these higher-mass galaxies dominate the sample, whereas the Main Galaxy Sample is dominated by lower-mass galaxies. Because of these key differences, the impact of assembly bias in our models will be qualitatively different compared to H13 (see Section 6).

In Paper II we will use the actual colour distributions of massive galaxies as a function of redshift to perform age matching. Our goal in this paper, however, is to perform a first qualitative analysis of the general effects of age matching above collapse mass, a regime that has not yet been fully investigated. For this purpose, we introduce a simple colour-rank distribution denoted $X_{\rm col}$. This colour-rank distribution will be used to assign 'colours' to CMASS and to non-CMASS galaxies and to perform the colour-based rank ordering in the age matching scheme. Our goal is to construct a model that allows for a simple 'mixing' between these two populations.

Operationally, we accomplish this mixing with our age matching model as follows. First, at each stellar mass we generate a random distribution of $X_{\rm col}$ values. Suppose there are $N_{\rm h}$ subhaloes in the stellar mass bin, and that the fraction of galaxies of this stellar mass that are CMASS-selected is denoted by $f_{\rm CMASS}$. We then draw $f_{\rm CMASS} \times N_{\rm h}$ values from a Gaussian distribution of mean $\mu_{\rm CMASS}$ and unit variance; these draws will be the 'colours' $X_{\rm col}$ of our mock CMASS galaxies. We next draw $(1 - f_{\rm CMASS}) \times N_{\rm h}$ values from a Gaussian distribution of *zero* mean and unit variance; these draws will be the 'colours' $X_{\rm col}$ of our non-CMASS galaxies. We then rank-order the joint collection of the randomly drawn values of $X_{\rm col}$. Subhaloes in the same stellar mass bin are rank-ordered by $z_{\rm starve}$. In monotonic fashion, the larger $X_{\rm col}$ draws are assigned to the subhaloes with larger $z_{\rm starve}$ values, and the CMASS-designation associated with $X_{\rm col}$ is also assigned to the subhalo, defining the CMASS selection function in the 'AgM' model.

The value of $\mu_{\rm CMASS}$ determines the strength of the correlation between the CMASS selection function and subhalo $z_{\rm starve}$ at fixed stellar mass. If $\mu_{\rm CMASS}$ is large (for instance, $\mu_{\rm CMASS} = 10$), then $X_{\rm col}$ −values with a CMASS-designation are always larger than $X_{\rm col}$ −values attached to non-CMASS draws, in which case at fixed stellar mass, subhaloes with the highest $z_{\rm starve}$ are always selected to be CMASS galaxies. On the other hand, if $\mu_{\rm CMASS} = 0$, the $X_{\rm col}$

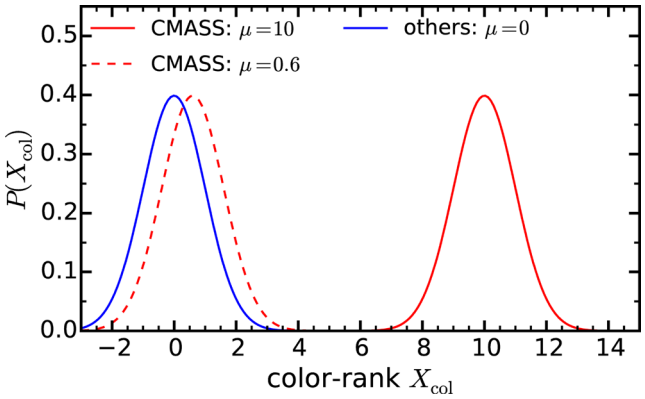

Figure 2. Illustrative figure of the colour–rank distributions for CMASS and non-CMASS galaxies. The $X_{\rm col}$ 'colours' of non-CMASS galaxies are drawn from a normal distribution with unit variance and zero mean (shown by the solid blue line). The $X_{\rm col}$ 'colours' of CMASS galaxies are drawn from a normal distribution with unit variance and with a mean value equal to $\mu_{\rm CMASS}$. When $\mu_{\rm CMASS} = 0.599$ (dashed red line), CMASS and non-CMASS galaxies have overlapping colour distributions but CMASS is redder on average. When $\mu_{\rm CMASS} = 10$ (solid red line), all CMASS galaxies are redder than non-CMASS galaxies (this situation corresponds to the extreme age-matching case explored in Section 6.3). Our best-fitting value for $\mu_{\rm CMASS}$ is 0.599 and corresponds to the distribution shown by the dashed red line.

distributions of CMASS and non-CMASS draws are identical, so in this case matching the $X_{\rm col}$ and $z_{\rm starve}$ distributions has no impact on the CMASS designation assigned to the subhaloes, and the CMASS selection function is uncorrelated with $z_{\rm starve}$ at fixed stellar mass. Finally, for intermediate values of $\mu_{\rm CMASS}$ (for instance, $\mu_{\rm CMASS} = 0.6$), then CMASS and non-CMASS galaxies have overlapping $X_{\rm col}$ distributions, but CMASS galaxies are 'redder' on average. Fig. 2 illustrates these concepts.

In our analysis, $\mu_{\rm CMASS}$ is left as a free parameter which means that we determine the degree to which CMASS colours overlap with non CMASS galaxies directly from the data. We do not however currently account for any redshift and stellar-mass dependence of $\mu_{\rm CMASS}$, thus we do not account for any redshift and stellar-mass dependence of the CMASS colour-cuts. This is a limitation of our current model, the importance of which will become clearer in Section 6.3.

5.4 Accounting for the stellar mass completeness of CMASS as a function of redshift

We assume a single global SMF over the CMASS redshift range. For each set of parameters (ϕ_1, M_0, σ), we create a mock catalogue via abundance matching. At this point galaxies in the mock catalogue have redshifts and stellar masses. The next step is to tag CMASS galaxies in the abundance-matched mock catalogue as a function of redshift. We divide our simulation into seven redshift bins along the Z direction (the bin width is $\Delta z = 0.04$). The redshift width of $\Delta z = 0.04$ is conservative and this choice is motivated by the uncertainty of photometric redshift estimation in the s82-MGC catalogue.

The CMASS SMF varies as a function of redshift as a result of the BOSS selection function. In Section 3.3, we used the s82-MGC catalogue to measure the number densities of CMASS galaxies as a function of mass and redshift, $N^{\rm CMASS}_{\rm sim}(M_*, z)$. Because we assume that the total SMF does not vary over our redshift baseline, we can compute how many CMASS galaxies are expected for every redshift slice in the mock catalogue simply by scaling this number by the ratio of volume in the redshift slice in the mock ($\Delta V_{\rm sim}(z)$) to the s82-MGC volume ($\Delta V_{\rm S82}(z)$):

$$N^{\rm CMASS}_{\rm sim}(M_*, z) = \frac{\Delta V_{\rm sim}(z)}{\Delta V_{\rm S82}(z)} N^{\rm CMASS}_{\rm S82}(M_*, z). \quad (9)$$

In order to predict the number of mock galaxies as a function of mass and redshift, we construct bins in stellar mass from 10.6 to 12.3 dex with $\Delta \log M_* = 0.05$. We have checked that our prediction is stable with $\Delta \log M_* = 0.1$. In the mock catalogue, we randomly tag $N_{\rm CMASS}(M_*, z)$ galaxies with a CMASS flag. For a small number of bins, $N^{\rm CMASS}_{\rm sim}(M_*, z)$ exceeds the number predicted by the total SMF (simply due to sample variance). In this case, we simply set $N^{\rm CMASS} = N^{\rm tot}$. Following this procedure, every galaxy in our mock catalogue is now assigned a stellar mass, a redshift, and a flag that indicates mock CMASS galaxies. By design, mock CMASS galaxies have stellar mass distributions that match the ones measured in Section 3.3.

5.5 Predicting the CMASS two-point correlation function

We now have a mock catalogue that contains galaxies with three dimensional positions and with a flag that indicates CMASS galaxies. The next step is to compute the predicted the CMASS two-point correlation function. $w_{\rm p,\,theory}$ is computed from the mock following the exact same procedure as for the BOSS DR10 data. To account for the finite volume of the simulation, we compute a covariance matrix for $w_{\rm p,\,theory}$ (referred to as $\boldsymbol{C}_{w_{\rm p},{\rm theory}}$), which is estimated via jack-knife by dividing the (X, Y)-plane into 256 equal regions. For the small scales of concern in this paper, jack-knife errors outperform bootstrap errors (P. Norberg, private communication; Arnalte-Mur & Norberg et al., in preparation).

The fitting for $w_{\rm p}$ is performed with

$$\chi^2_{w_{\rm p}} = \sum_{i,j} \Delta_{w_{\rm p}}(r_{{\rm p},i}; \phi_1, M_0, \sigma) \boldsymbol{C}^{-1}_{w_{\rm p},{\rm total},ij} \Delta_{w_{\rm p}}(r_{{\rm p},j}; \phi_1, M_0, \sigma), \quad (10)$$

where $\Delta_{w_{\rm p}}(r_{{\rm p},i}; \phi_1, M_0, \sigma) = w_{\rm p,meas}(r_{{\rm p},i}) - w_{\rm p,theory}(r_{{\rm p},i}; \phi_1, M_0, \sigma)$, and the total covariance matrix includes uncertainties in both measurement and our theory estimates, i.e. $\boldsymbol{C}_{w_{\rm p},{\rm total}} = \boldsymbol{C}_{w_{\rm p},{\rm meas}} + \boldsymbol{C}_{w_{\rm p},{\rm theory}}$.

5.6 Summary of methodology

Fig. 3 presents an illustration of our methodology for the AbM model. A summary of our methodology is as follows.

(i) Start with a set of SMF parameter values. For the stochastic ('AbM') model, the parameters are (ϕ_1, M_0, σ). For the age-matching ('AgM') model there is an additional parameter, $\mu_{\rm CMASS}$. The parameter $\mu_{\rm CMASS}$ only impacts the modelling of two-point statistics such as $w_{\rm p}$ – one-point statistics such as the SMF are entirely unaffected by $\mu_{\rm CMASS}$.

(ii) The two parameters ϕ_1 and M_0 control the total SMF (without scatter). The total SMF including scatter is obtained analytically following equation (7). A $\chi^2_{\rm SMF}$ is computed between this analytic model and the total SMF estimated in Section 3.2.

(iii) In parallel, we generate a mock catalogue to model w_p. The first step in generating this mock catalogue is to abundance match the mock catalogue using the same total SMF (without scatter) as in the previous step. We test abundance matching both in terms of $V_{\rm peak}$ and $M_{\rm peak}$. Scatter (σ) is introduced into stellar mass in the mock catalogue at fixed $V_{\rm peak}$ (or $M_{\rm peak}$). We have checked that the

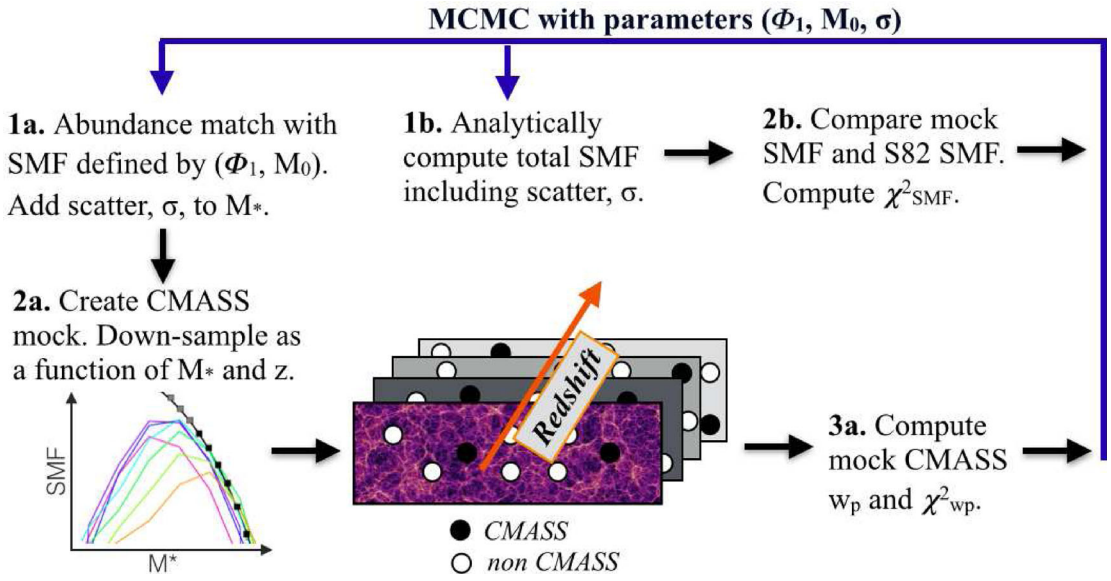

Figure 3. Illustration of our overall methodology for constraining the AbM model and creating a mock CMASS catalogue. The stochastic AbM model contains three free parameters: (ϕ_1, M_0, σ). The age-matching (AgM) model contains one additional parameter, $\mu_{\rm CMASS}$, which controls how strongly CMASS galaxies correlate with $z_{\rm starve}$ at fixed $V_{\rm peak}$.

mock catalogue is large enough that stochasticity due to the rare number of high-mass haloes is a negligible effect, i.e. the Poisson error in the measured mass function dominates the error budget at high stellar masses.

(iv) The Z direction of the mock is taken as the redshift axis. Mock CMASS galaxies are tagged in the mock catalogue by down-sampling the overall population in redshift and stellar mass in order to reproduce the CMASS SMFs measured in Section 3.3.

(v) At this stage, mock CMASS galaxies are simply a random sub-sample of the overall population; this mock corresponds to our stochastic 'AbM' model.

(vi) For the age-matching model, we begin by assigning the subhaloes a colour-rank, $X_{\rm col}$, as follows. For subhaloes hosting a non-CMASS galaxy, $X_{\rm col}$ is drawn from a Gaussian distribution with zero mean and unit variance. For subhaloes hosting a CMASS galaxy, $X_{\rm col}$ is drawn from a Gaussian distribution with mean $\mu_{\rm CMASS}$ and unit variance. At fixed stellar mass, the random $X_{\rm col}$ values are rank-ordered. At the same stellar mass, the mock galaxies are rank-ordered by a secondary halo property, where we choose $z_{\rm starve}$ as this secondary parameter in our fiducial model, where $z_{\rm starve}$ is concretely defined in Section 5.3. In monotonic fashion, the subhaloes with the largest $z_{\rm starve}$ values are assigned the largest $X_{\rm col}$ values, and the CMASS/non-CMASS designation associated with each $X_{\rm col}$ value is also assigned to the subhalo.[2] Thus subhaloes in the 'AbM' and 'AgM' mocks in general have different CMASS-designations: in 'AgM', the CMASS-designation is correlated with $z_{\rm starve}$ at fixed $V_{\rm peak}$, with the correlation strength governed by our $\mu_{\rm CMASS}$ parameter.

(vii) Generate a random catalogue that follows the CMASS dn/dz and compute $w_{\rm p,\,theory}$. Note that $\boldsymbol{C}_{\rm theory}$ is fixed using our best-fitting parameters (after a first initial iteration).

(viii) Compute $\chi^2_{\rm w_p}$ between $w_{\rm p,\,meas}$ and $w_{\rm p,\,theory}$, and then add as $\chi^2 = \chi^2_{\rm SMF} + \chi^2_{\rm w_p}$.

[2] For certain tests, we may rank-order the subhaloes only according to $z_{\rm form}$ or $z_{\rm char}$ (Section 5.3).

(ix) Iterate this procedure.

The best-fitting parameters and errors are determined using the Markov chain Monte Carlo (MCMC) technique. We use a modified version of COSMOMC (Lewis & Bridle 2002) that has been well tested in previous work (Saito, Takada & Taruya 2011; Zhao et al. 2013; Saito et al. 2014). Since our SMF is estimated from S82-MGC and the correlation function $w_{\rm p}$ is computed over the full DR10 footprint, the cross-correlation between these two statistics are negligible. The χ^2 for the multipoles is defined in a similar way. The correlation between the monopole and the quadrupole is properly taken into account by the covariance matrix.

6 RESULTS

6.1 Abundance matching

We now perform a joint fit to the SMF and to $w_{\rm p}$. The left-hand panel of Fig. 4 presents our best fit to the SMF using a double Schechter function and abundance-matching against $V_{\rm peak}$. The best-fitting parameters for the double Schechter function are: $(\phi_1, \log_{10} M_0, \sigma) = (1.86^{+0.21}_{-0.61} \times 10^{-3}, 10.89^{+0.05}_{-0.04}, 0.105^{+0.024}_{-0.032})$ with $\chi^2_{\rm SMF} = 4.55$. Errors are reported with a 68 per cent confidence level. We find excellent fits to both the SMF and $w_{\rm p}$ with two specific points worth highlighting. First, the amplitude of our best-fitting SMF agrees well with COSMOS and PRIMUS at $\log_{10} M_* \gtrsim 11.0$ but has a lower amplitude at $\log_{10} M_* \lesssim 11.0$. Because the number density of CMASS drops sharply below this mass scale, we simply do not expect to constrain the total SMF in this range. Secondly, the best-fitting value for the scatter is lower than our naive expectation. Indeed, σ should include contributions from measurements errors as well as from intrinsic scatter in the stellar-to-halo mass relation. The average uncertainty in stellar mass measurements from the S82-MGC is of order $\sigma_{\rm meas} \sim 0.1$ dex in this mass and redshift range. Hence, a value of $\sigma = 0.105$ implies a very small *intrinsic* scatter in the stellar-to-halo mass relation. We will return to this point in the discussion section.

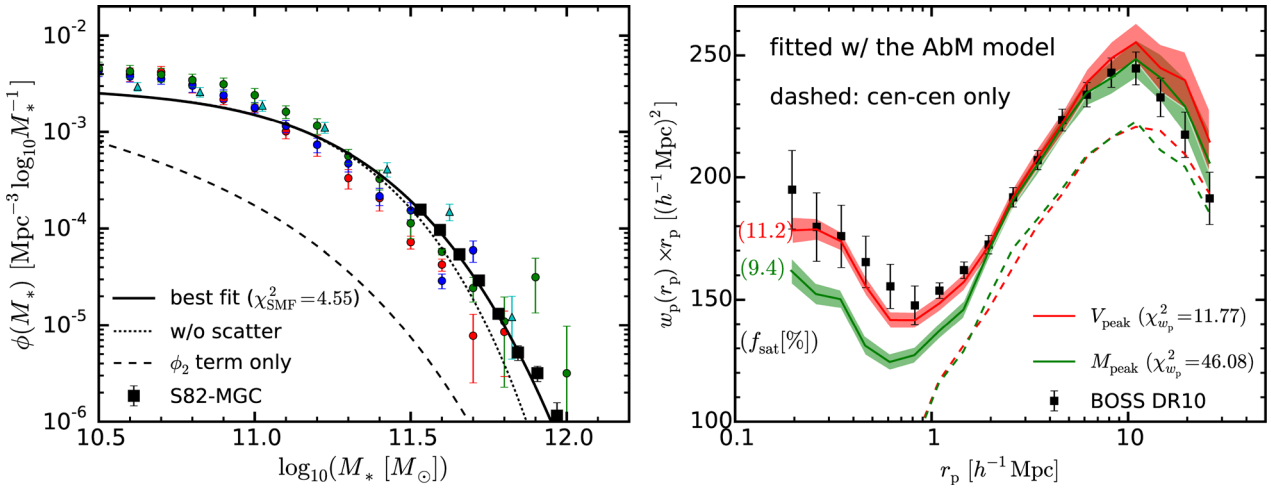

Figure 4. (Left) Best fit to the s82-MGC SMF for the AbM model (solid black line). The dotted black line corresponds to the SMF deconvolved for scatter. The black dashed curved shows the (fixed) ϕ_2 term in our double Schechter function. Black squares correspond to the measured SMF from the s82-MGC. (Right) Our best fit to $w_{\rm p}$ for the AbM model (solid red line). The green line shows the result of abundance matching against $M_{\rm peak}$ instead of $V_{\rm peak}$. Dashed lines display the contribution to $w_{\rm p}$ from central-central pairs. Numbers in parenthesis indicate satellite fractions (11.1 per cent for $V_{\rm peak}$ and 9.5 per cent for $M_{\rm peak}$). The goodness of fit for the AbM model is $\Delta\chi^2 = (4.55 + 11.77)/(26 - 3) = 0.710$.

The right-hand panel of Fig. 4 presents our best fit to $w_{\rm p}$ as the red line ($\chi^2_{w_{\rm p}} = 11.43$). The goodness of fit in this case is $\chi^2/({\rm d.o.f.}) = (4.55 + 11.77)/(8 + 18 - 3) = 0.710$. We have also tested abundance matching against $M_{\rm peak}$ instead of $V_{\rm peak}$. The blue line shows the results of abundance matching against $M_{\rm peak}$ using the same best-fitting SMF parameters as above. As can be seen from Fig. 4, $V_{\rm peak}$ yields a larger clustering amplitude and is more consistent with the BOSS data than $M_{\rm peak}$.

There are two factors which lead to the differences in these clustering predictions. First, host haloes selected by $M_{\rm peak}$ cluster more weakly relative to host haloes selected by $V_{\rm peak}$, as discussed in Zentner, Hearin & van den Bosch (2014). This effect is small in our halo mass range, which we have verified by comparing the central–central pair counts between the two models, which are nearly identical. Secondly, the satellite fractions predicted by the two models are different: our $V_{\rm peak}$−based SHAM model has a larger satellite fraction relative to the $M_{\rm peak}$−based model. Indeed, at fixed $M_{\rm peak}$, subhaloes have larger $V_{\rm peak}$ than host haloes (see fig. 2 in Reddick et al. 2013), which suggests that rank-ordering with $V_{\rm peak}$ results in similar clustering of central galaxies but the larger satellite fraction boosts the overall clustering amplitude. We adopt $V_{\rm peak}$ as our fiducial model and do not explore abundance matching with $M_{\rm peak}$ any further.

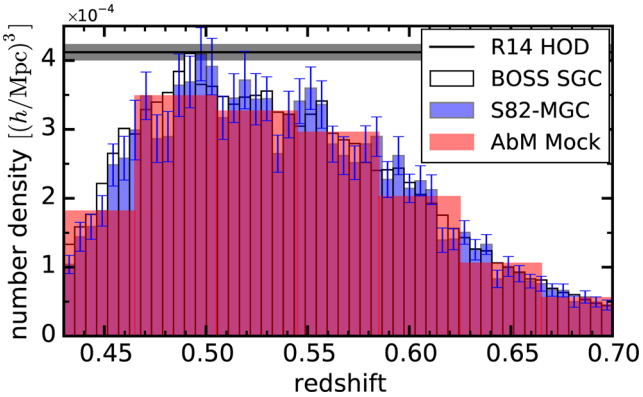

Figure 5. Comparison between the CMASS dn/dz from our fiducial mock catalogue (red histograms), the measured dn/dz from the s82-MGC (blue histograms), and the measured dn/dz from the full BOSS DR10 SGC (white histograms, Anderson et al. (2014)). Errors on the dn/dz for the s82-MGC are estimated via bootstrap. For the DR10 SGC dn/dz, redshift failures and fibre-collided galaxies are included using a nearest-neighbour weighting scheme (see Anderson et al. 2014). By construction, our models reproduce the redshift distribution of CMASS galaxies from the s82-MGC catalogue which is in turn consistent with the DR10 SGC CMASS redshift distribution. The number density from the fiducial R14 model is shown as a horizontal solid black line. In the R14 model, the CMASS dn/dz is reproduced by randomly downsampling a fixed redshift independent HOD.

6.2 CMASS dn/dz

Fig. 5 presents a comparison between the redshift distribution of CMASS galaxies from our best-fitting mock catalogue with the redshift distribution of CMASS galaxies in the s82-MGC and from the full BOSS DR10 SGC. Our mock reproduces the CMASS dn/dz from the s82-MGC catalogue and is consistent with dn/dz from the BOSS DR10 SGC. The amplitude differences between the dn/dz from our mock and the DR10 dn/dz are due to sample variance. In our current methodology, the sample variance introduced by matching the CMASS SMFs from Stripe 82 is not taken into account which is a limitation of our current approach. This reflects a trade-off made to take advantage of the higher quality stellar mass estimates from the s82-MGC, but doing so, our current analysis is also limited by the sample variance from Stripe 82.

6.3 Gaining an intuition for age matching above collapse mass

In the previous section, we showed that a reasonable fit to Φ and $w_{\rm p}$ can be achieved using a simple abundance matching scheme in which galaxy colour in high-mass haloes is simply a stochastic process. We now investigate whether or not models in which galaxy colour *correlates* with halo assembly properties can achieve comparable results. One caution worth mentioning here with respect to the age matching model is that, unlike in H13, the combination of the

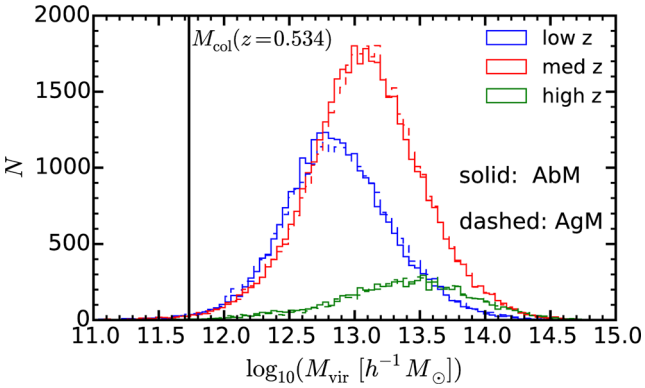

Figure 6. Halo mass histograms as a function of redshift from our AbM (solid lines) and AgM (dashed lines) mock catalogues. Collapse mass at $z = 0.534$ is indicated by a black solid vertical line. Clearly, CMASS galaxies populate haloes with masses firmly above collapse mass. Also note that the mean halo mass of CMASS in our mocks varies by a factor of 3.5 from low to high redshift.

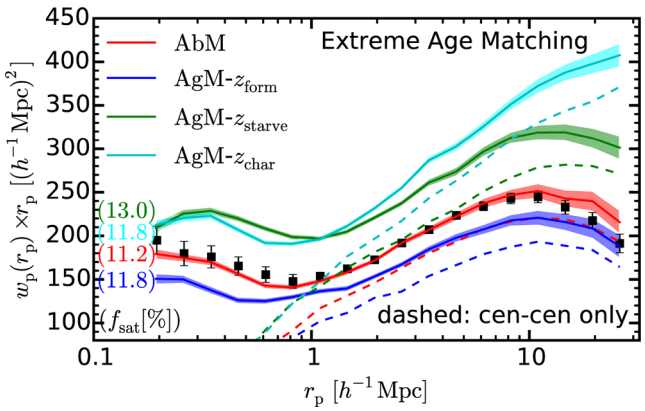

Figure 7. Impact of age matching (AgM model) on $w_{\rm p}$ for an extreme scenario with $\mu_{\rm CMASS} = 10$ (CMASS galaxies are redder than all other galaxies). Rank ordering is performed versus $z_{\rm form}$ (blue), $z_{\rm starve}$ (green) and $z_{\rm char}$ (cyan). For comparison, we also present the best-fitting curves from the AbM model (red solid line) in which the correlation between the colours of CMASS galaxies and subhalo age is completely stochastic. This goal of this figure is simply to highlight the qualitative trends of age-matching above collapse mass. Rank ordering versus $z_{\rm char}$ increases the amplitude of $w_{\rm p}$ whereas rank ordering versus $z_{\rm form}$ decreases the amplitude of $w_{\rm p}$. Dashed lines show the contribution to $w_{\rm p}$ from central–central pairs. Numbers in parenthesis indicate satellite fractions.

steep $V_{\rm peak} - M_*$ relation and the non-zero scatter in this relation leads to a difference in the mean host halo mass compared to the standard abundance matching model (see Appendix B for details).

First, we wish to develop some intuition for how the different components of $z_{\rm starve}$ affect $w_{\rm p}$ in this high halo mass regime. Fig. 6 shows that CMASS galaxies are firmly in halo masses above collapse mass, $M_{\rm col}(z = 0.534) = 10^{11.73}\,h^{-1}\ {\rm M}_\odot$. Hence, the behaviour of $z_{\rm starve}$ may be fundamentally different compared to previous work by H13. Let us begin by considering an extreme case in which CMASS galaxies are all redder than non-CMASS galaxies ($X_{\rm col,\,CMASS} \gg X_{\rm col,\,others}$, see solid lines in Fig. 2). For this test, we adopt the values of the best fit to Φ from Fig. 4. At fixed stellar mass, we rank order galaxies according to $z_{\rm starve}$, $z_{\rm form}$, or $z_{\rm char}$. The results of this extreme case are presented in Fig. 7. Interestingly, but perhaps not surprisingly, we find that $z_{\rm form}$ (blue curve) *lowers* the clustering amplitude. This is because $z_{\rm form}$ is defined using halo

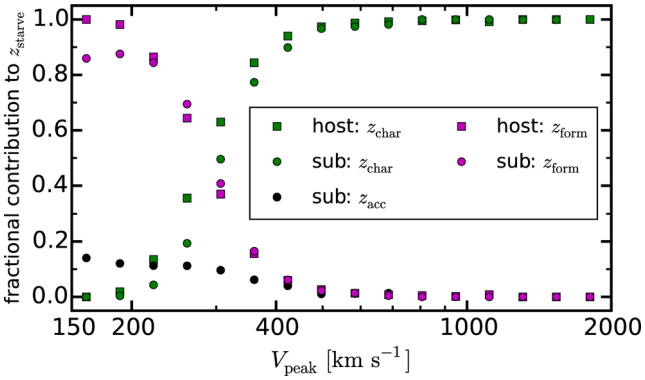

Figure 8. Fractional contribution to $z_{\rm starve}$ as a function of $V_{\rm peak}$ at $z = 0.534$ for host (square) and sub (circle) haloes. The $z_{\rm char}$ term dominates at the high-mass end whereas the $z_{\rm form}$ term dominates at the low-mass end.

concentrations and the effects of assembly bias have an opposite effect above and below collapse mass when using the concentration parameter (see e.g. Wechsler et al. 2006; Dalal et al. 2008). Thus, in this high-mass regime, $z_{\rm form}$ causes red galaxies to cluster *less* strongly than blue ones.

Let us now turn our attention to $z_{\rm char}$. Interestingly, rank ordering according to $z_{\rm char}$ produces the opposite effect and causes an *increase* in the clustering amplitude. Previous work on assembly bias has shown the switch in the assembly bias effect seen when considering halo concentration is not always reflected when considering other halo parameters. Previous work has not studied the specific case of $z_{\rm starve}$; however, Jing et al. (2007) and Li et al. (2008) report that when an age parameter based on a fixed mass threshold such as $z_{1/2}$ is used where $z_{1/2}$ denotes the redshift when a halo acquires half of the final mass at the observational time, a similar behaviour is observed (see fig. 4 in Li et al. 2008).

Finally, let us now examine the $z_{\rm starve}$ component, which includes contributions from both $z_{\rm char}$ and $z_{\rm form}$. The prediction for $z_{\rm starve}$ lies between the $z_{\rm form}$ and the $z_{\rm char}$ cases but is closer to $z_{\rm char}$ than to $z_{\rm form}$. This is because in this mass regime, $z_{\rm starve}$ is dominated by $z_{\rm char}$ not $z_{\rm form}$ (see Fig. 8). Thus the impact of the assembly bias for CMASS is qualitatively distinct from the trends identified by H13 in lower mass haloes, a fact which traces to the change in character of assembly bias for haloes above and below collapse mass.

The dashed curves in Fig. 7 display $w_{\rm p}$ for central galaxies only – demonstrating that the trends discussed above are not simply due to varying satellite fractions.

6.4 Fit to w_p with an age matching type model

Of course, the true differences between the colour distributions of CMASS galaxies compared to non-CMASS galaxies of similar mass are not as extreme as the case explored in the previous section. As discussed in Section 5.1, the implementation of age-matching first requires a characterization of the colour distributions of galaxies from the s82-MGC as a function of mass and redshift and also requires modelling the effects of scatter introduced in these colour distributions from photometric redshifts. This is an aspect that we defer to Paper II. Here, we perform a *qualitative* investigation of the effects of age matching on the two-point correlation function using the colour-rank variable $\mu_{\rm CMASS}$.

We now perform a joint fit to the SMF and to $w_{\rm p}$ in which $\mu_{\rm CMASS}$ is left as a free parameter (the 'AgM' model). The results are presented in Fig. 9. The best-fitting parameters

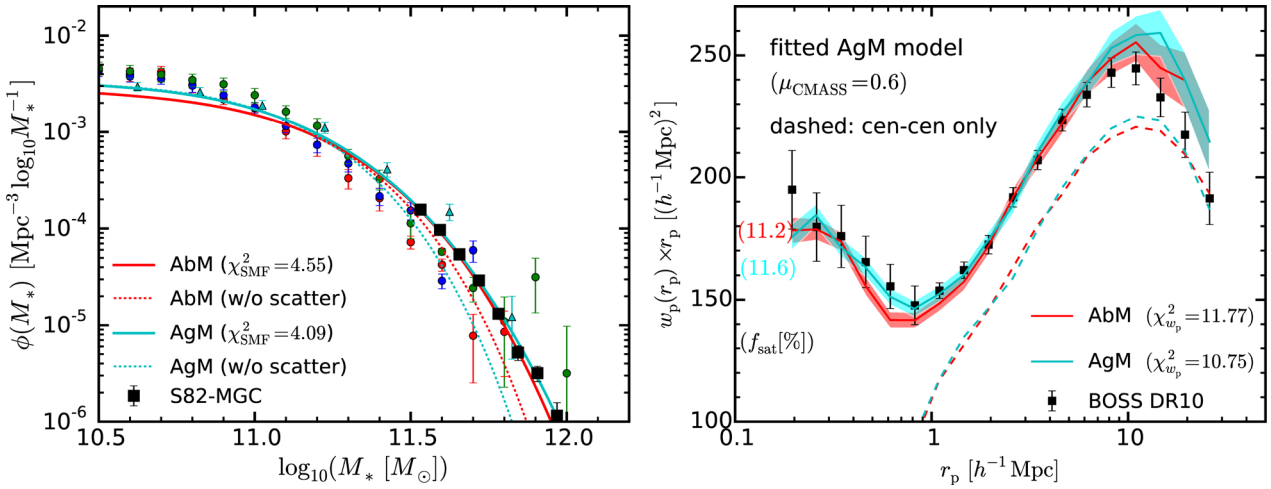

Figure 9. (Left) Our best fit to the s82-MGC SMF for the AgM model (solid cyan line). The dotted cyan line corresponds to the SMF deconvolved for scatter. For comparison, the AbM result is displayed with red lines. Black squares correspond to the measured SMF from the s82-MGC. (Right) Our best fit to $w_{\rm p}$ for the AgM model (solid cyan line). For comparison, the AbM result is shown as a red solid line. Dashed lines display the contribution to $w_{\rm p}$ from central–central pairs. Numbers in parenthesis indicate satellite fractions. The goodness of fit for the AgM model is $\Delta\chi^2 = (4.09 + 10.75)/(26 - 4) = 0.674$.

are $(\phi_1, \log_{10} M_0, \sigma, \mu_{\rm CMASS}) = (2.51^{+1.71}_{-0.75} \times 10^{-3}, 10.83^{+0.04}_{-0.11}, 0.136^{+0.38}_{-0.22}, 0.599^{+0.435}_{-0.164})$ with $\chi^2_{\rm SMF} = 4.09$ and $\chi^2_{w_{\rm p}} = 10.75$. The AbM model and the AgM model yield a comparable goodness of fit ($\Delta\chi^2 = (4.55 + 11.77)/(26 - 3) = 0.710$ for the AbM model and $\Delta\chi^2 = (4.09 + 10.75)/(26 - 4) = 0.674$ for the AgM model). There are three points worth highlighting concerning the results of the AgM model. First, the best-fitting SMF has a slightly higher amplitude at low stellar masses compared to the AbM model and is in better agreement with PRIMUS and COSMOS. Secondly, the best-fitting value for the scatter is larger than the AbM model ($\sigma = 0.136$ versus $\sigma = 0.105$), which leaves a larger margin for intrinsic scatter. Finally, the best-fitting value for $\mu_{\rm CMASS}$ of 0.599 corresponds to a scenario in which CMASS and non-CMASS galaxies have overlapping colour distributions, but with CMASS galaxies being somewhat redder on average. Reassuringly, this result matches our qualitative expectations for this sample.

The AgM model explored here is simplistic in the sense that we have used a single value of $\mu_{\rm CMASS}$ over a whole CMASS redshift range, whereas the true colour distribution of CMASS versus other galaxies depends on redshift. A more sophisticated model which accounts for this effect will be presented in a forthcoming paper.

7 DISCUSSION

7.1 HOD modelling in the context of complex samples such as CMASS

Both HOD and SHAM are popular methods for modelling the SMF and the galaxy-two-point correlation functions. One reason that HOD methods are popular is that they provide a relatively simple framework that can also be used to rapidly model a variety of observables. However, one of the downsides of this method is that specific functional forms must be assumed for the central and satellite occupation functions. These assumptions may be robust for volume-limited threshold samples such as those commonly studied in the SDSS main samples (e.g. Zehavi et al. 2011). However, it is less clear if these types of methods can be applied to samples such as CMASS which are selected via complex colour and luminosity cuts and for which both the shape and normalization of the effective HOD may vary with redshift.

There have been several attempts to model the CMASS-halo connection on the basis of HOD type models. Among these studies, Guo et al. (2013, 2014) and More et al. (2015) focused on specific sub-samples of CMASS, whereas White et al. (2011) and R14 used a HOD type model to describe the clustering of the full CMASS, assuming no redshift evolution in the HOD.

In this paper, we have introduced a novel SHAM-based method[3] that can be used to model complex populations such as CMASS by accounting for the mass completeness of the sample as a function of redshift. We explore a first qualitative approach for also considering colour completeness which will be developed further in Paper II. We now investigate what these models predict in terms of the redshift dependence of the CMASS HOD. The right-hand panel of Fig. 1 shows that the SMF of CMASS varies strongly with redshift. This figure alone suggests that the HOD of the CMASS sample is not likely to be uniform over the CMASS redshift range.

Fig. 10 s presents the HODs predicted from our AbM and AgM mock catalogues as a function of redshift. As a comparison we also display the HOD from R14, which assumes no redshift evolution. R14 fit the clustering assuming a constant number density with a derived value of $\overline{n} = (4.12 \pm 0.13) \times 10^{-4}\,(h^{-1}\,{\rm Mpc})^{-3}$ (see Fig. 5) under the assumption that the CMASS dn/dz can be obtained by simply downsampling the best-fitting HOD as a function of redshift. We downsample the R14 HOD to match the CMASS dn/dz and present the results in Fig. 10.

There are several noteworthy differences between our HODs and the single non-evolving one from R14. At the lowest redshift bin, $z = 0.445$, the mean occupation for central galaxies does not approach unity due to incompleteness in the SMF at high-mass end (see the magenta curve in the right-hand panel of Fig. 1). At $z = 0.565$, which corresponds to the peak of the CMASS dn/dz, our HOD is more similar to R14, but there is still a discrepancy in the shape of $\langle N_{\rm cen}\rangle$, especially at the low-mass end. The largest

[3] After this paper was submitted, a parallel effort was brought to our attention which adopts a similar methodology as our paper (Rodríguez-Torres et al. 2016).

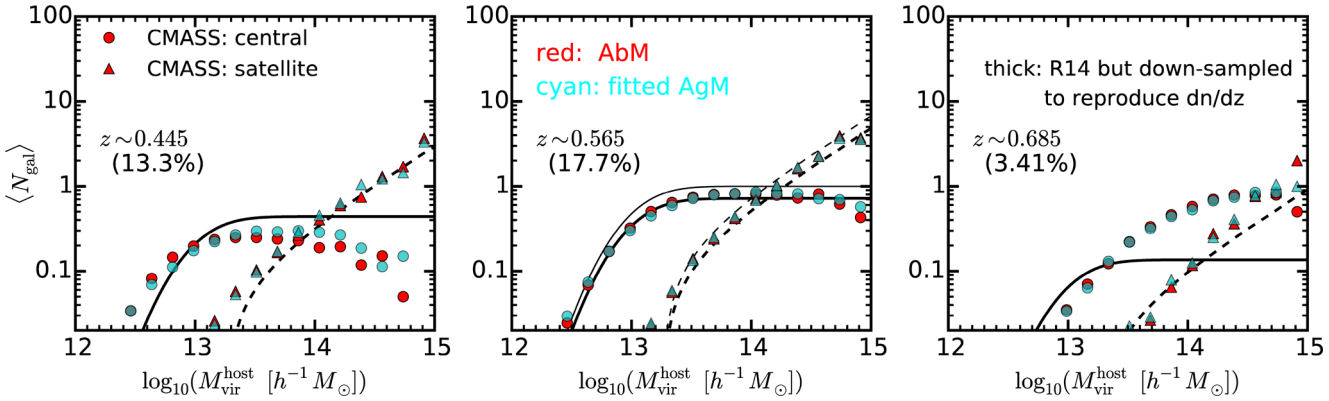

Figure 10. Redshift dependent CMASS HODs from our AbM (red circles and triangles) and AgM (cyan circles and triangles) mock catalogues. The thin black lines in the middle panel correspond to the fiducial R14 CMASS HOD. Note that the virial halo mass in R14 is converted to the Rockstar one. The solid line represents centrals and the dashed line represents satellites. Our models should be compared with the thick black lines which correspond to the R14 CMASS HOD after downsampling to match the CMASS dn/dz. Numbers in parenthesis represent the percentage of CMASS galaxies in each redshift bin compared to the full sample. The data of the HOD table as a function of redshift will be made publicly available at www.massivegalaxies.com.

differences are at $z > 0.6$. Our HODs converge to unity at large halo masses whereas the downsampled R14 one converges to $N_{\rm tot} \sim 0.1$; this is due to the stellar mass completeness of CMASS. This difference arises, because, in our models, the decline of the CMASS number density above $z = 0.55$ is caused by the fact that the mean stellar mass of the sample increases (as constrained by data from the s82-MGC). In contrast, the fixed HOD of R14 must significantly downsample the overall amplitude of the HOD to achieve comparable number densities.

Finally, our model predicts an evolution of the mean halo mass of CMASS, as a function of redshift. More specifically, our models predict that, at $z = 0.445$, 0.565 and 0.685, the mean halo mass of central CMASS galaxies is $\log_{10}(\overline{M}_{\rm halo}\,[h^{-1}\,{\rm M}_\odot]) = 13.12\,(13.15)$, 13.34 (13.35), and 13.66 (13.68) for the abundance-matched (age-matched) cases, respectively. This variation is driven by the fact that mean stellar mass of the sample varies with redshift, as is clearly seen in the right-hand panel of Fig. 1. These values are compared with the HOD result, $\log_{10}(\overline{M}_{\rm halo}\,[h^{-1}\,{\rm M}_\odot]) = 13.51$, which is higher (lower) than our results at low (high) redshift. In addition, our models predict that the CMASS satellite fraction varies with redshift from 12 per cent to 9 per cent, as shown in Fig. 11. While this effect might seem like a small and negligible variation, the fiducial HOD from R14 constrains the satellite fraction at 6.8 per cent precision. It is interesting that the value inferred from the single HOD fit in R14 is consistent with our values at $z \sim 0.6$ but that not at lower redshifts.

In conclusion, our work suggests that CMASS is a complex sample for which the HODs are likely to vary with redshift in a non-trivial manner. A single HOD fit to the overall $w_{\rm p}$ broadly agrees with the predictions from our model at the median redshift of the sample. However, at lower and higher redshifts, our model predicts that HODs are not simple downsampled versions of the HOD at the peak of the dn/dz.

7.2 A cautionary tale of modelling small-scale statistics

Many previous studies have used a combination of galaxy abundances and the projected galaxy two-point correlation function in order to constrain the galaxy-halo connection (e.g. Leauthaud et al. 2011; Coupon et al. 2015; Zu & Mandelbaum 2016). However, just because SHAM or HOD models can reproduce these observables does not necessarily imply that the models accurately capture the

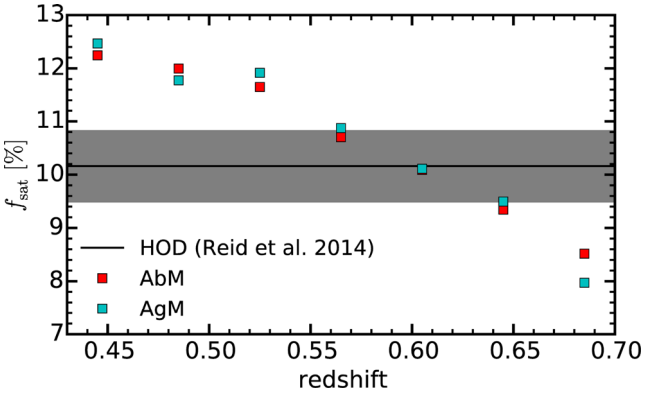

Figure 11. Redshift evolution of the satellite fraction predicted from our AbM (red squares) and AgM (blue squares) models. The redshift independent satellite fraction from R14 is shown as a horizontal black line. The grey shaded region indicates the 1σ error on the R14 satellite fraction. The satellite fraction in our SHAM models evolves with redshift and is only consistent with R14 at $z \sim 0.6$.

true underlying galaxy halo connection, i.e. just because the model provides a good fit to the data does not necessarily imply that the model is correct. A clear illustration of this statement in the context of mock galaxy samples with strong assembly bias is discussed in Zentner et al. (2014). In this paper, we have studied two distinct models: standard abundance matching and a simplified form of age matching, abbreviated by AbM and AgM, respectively. We have demonstrated that both models can reproduce the galaxy SMF as well as $w_{\rm p}$, suggesting that there are fundamental degeneracies among traditional HOD model, AbM, and AgM models, in modelling the SMF and $w_{\rm p}$. This naturally leads to two interesting and inter-related questions.

(i) How well do these models predict other statistics derived from the data?

(ii) Are there other statistics which can distinguish between these two distinct models?

Instead of considering just the projected correlation function, we turn our attention to the multipoles of the full 2D correlation function. Fig. 12 shows the pseudo multipoles (see Section 3) for our best-fitting AbM and AgM models. The left-hand panel of Fig. 12

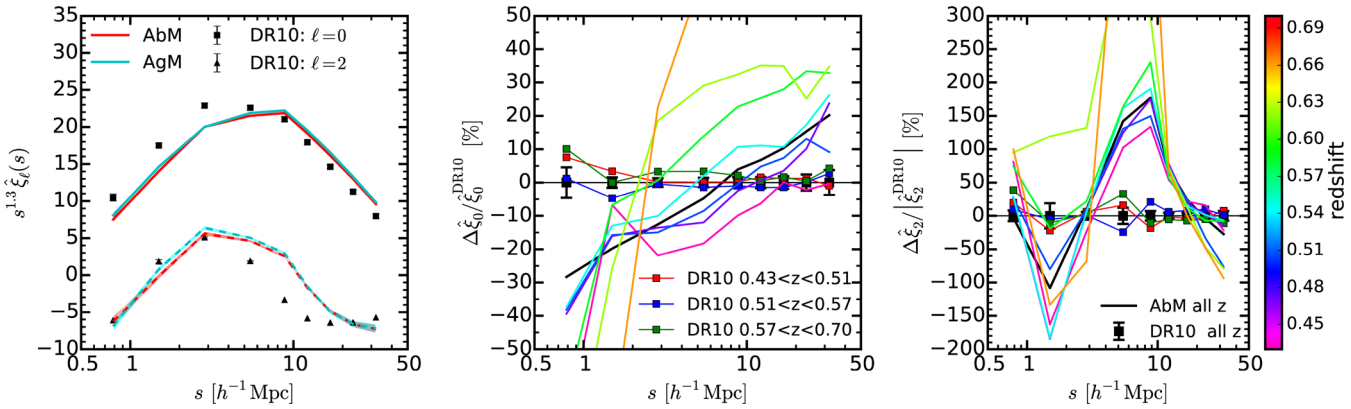

Figure 12. Left-hand panel: comparison between the measured CMASS pseudo multipoles from R14 and the prediction from our AbM and AgM mock catalogues. Solid lines correspond to the pseudo monopole and dashed lines correspond to the pseudo quadrupole. Neither the AbM or the AgM model are able to reproduce the BOSS measurements. Note that our errors on the pseudo multipoles looks smaller than ones in R14 because only measurement errors are included here. Middle panel: redshift evolution of pseudo multipoles in the AbM model prediction are shown as a fractional difference with respect to the measurement for the full sample. Red, blue, and green squares correspond to BOSS measurements in three different redshift bins. The measured BOSS pseudo multipoles display almost no variation with redshift. In stark contrast with the BOSS measurements, our models (solid coloured lines) predict a significant evolution in the pseudo multipoles, driven by the fact that the mean stellar mass of CMASS increases by a factor of 1.8 over the range $0.43 < z < 0.7$.

demonstrates that *both models fail dramatically to reproduce the pseudo multipoles* even though both models provide a satisfactory description of w_p. In the following section, we will use the redshift dependent clustering of CMASS to argue that in addition to stellar mass, galaxy colour must play an important role in determining the clustering of CMASS galaxies and that the failure of our model in reproducing the pseudo-multipoles must be a consequence of these effects.

In conclusion, our paper provides a clear cautionary example of the limitation of inferring the galaxy-halo connection from the projected correlation function alone. It is also clear from Fig. 12 that the pseudo-multipoles contain additional information not captured by w_p and that these may represent a powerful and under-utilized tool to provide additional constraints on the galaxy-halo connection. These aspects will be explored in greater detail in a forthcoming paper.

7.3 Redshift evolution of CMASS clustering

As discussed in Section 7.1, one major difference between the R14 model and this work is the treatment of the redshift evolution of the CMASS sample. In R14, CMASS is assumed to be a single homogenous sample with a $\mathrm{d}n/\mathrm{d}z$ that is modelled by downsampling a redshift independent HOD. In contrast, in this paper, the varying number density of CMASS is a direct result of the measured mass incompleteness of the sample as constrained by the 82-MGC catalogue. We now explore the consequences of these differences by examining the redshift dependent clustering of CMASS.

The original motivation for the non-evolving HOD in R14 originates from the observation that the clustering of CMASS galaxies does not vary strongly with redshift. This is shown by fig. A1 in R14 (reproduced here in the right two panels of Fig. 12). Because randomly downsampling galaxies does not modify their clustering, the R14 model leads to a constant clustering amplitude with redshift, which indeed, seems well supported by Fig. 12. However, another consequence of this procedure is that the halo mass of the CMASS sample is constant with redshift in the R14 model. In contrast, the s82-MCG catalogue shows that the *stellar mass* of the CMASS sample increases by a factor of 1.8 over the range $0.43 < z < 0.7$ which leads to a factor of 3.5 increase in the predicted mean halo mass of CMASS based on our SHAM modelling.

How much redshift evolution should we expect in the clustering of CMASS galaxies given this factor of 1.8 increase in stellar mass? The right hand side of Fig. 12 presents the predicted redshift evolution of the pseudo-multipoles from our SHAM modelling. We find that the observed stellar mass variation of the CMASS sample should lead to more than a factor of 1.5 increase in the clustering amplitude over the CMASS redshift range.[4] Fig. 12 clearly reveals a fundamental contrast between the measured non evolution of the clustering of CMASS and the expectation based on the redshift-dependent stellar mass distributions. This discrepancy is qualitatively insensitive to the exact details of our SHAM methodology. The observed increase in stellar mass will lead to a roughy similar increase in halo mass (and hence clustering amplitude) independently of the exact halo parameter (V_peak or M_peak) used in the abundance matching.

We argue that the discrepancy revealed in Fig. 12 suggests, in addition to stellar mass, *galaxy colour must also play an important role in determining the clustering amplitude of CMASS galaxies*. Fig. 5 in L16 demonstrates that CMASS galaxies display a range in star formation histories at fixed stellar mass. At low redshift and fixed stellar mass, the CMASS selection function excludes galaxies that have experienced recent star formation. At higher redshifts ($z > 0.6$), the CMASS sample is mainly flux limited and includes a larger range of galaxy colours at fixed magnitude. A variety of lensing and clustering studies suggest that, for low-mass galaxies, the clustering of blue galaxies is lower than red galaxies at fixed stellar mass (e.g. Tinker et al. 2013). It is not trivial that these trends persist in this very high galaxy mass regime, but if so, the inclusion of bluer galaxies in CMASS at higher redshifts may exactly compensate for the increase in the mean stellar mass. In other words, *the observed constant clustering of CMASS may be due to a coincidental compensation between colour and stellar mass with redshift.*

[4] Notice that we here ignore the redshift evolution in the MDR1 simulation. However, as seen in Fig. A1, the effect of the redshift evolution is at the level of 5 per cent.

7.4 What determines colour in the most massive galaxies?

One of the main goals of this paper is to understand the connection between halo properties and the colours of very massive galaxies. As shown in Fig. 6, CMASS galaxies live in haloes with halo masses above 10^{12} $M_\odot$. In this regime, gas accretion is thought to be dominated by the 'hot halo mode' and heated by pressure-supported shocks to a temperature that limits star formation (Dekel & Birnboim 2006). In addition, at these halo masses, 'maintenance mode' feedback mechanisms, such as radio-mode feedback, are thought to further limit star formation in the most massive galaxies Croton et al. (2006). However, massive galaxies at these redshifts are observationally not all red and dead. The CMASS sample in fact contains a blue population (Guo et al. 2013; Ross et al. 2013). Based on high-resolution *Hubble Space Telescope* imaging, Masters et al. (2011) estimate that ∼25 per cent of the CMASS sample has a late-type morphology associated with the star-forming disc (Masters et al. 2011). Using a maximum likelihood approach that accounts for photometric errors as well as the CMASS selection cuts, Montero-Dorta et al. (2014) estimate that 37 per cent of CMASS object may intrinsically belong to the blue cloud.

Semi-analytic models (SAMs) sometimes assume that galaxy colour in high-mass haloes is a stochastic process. For example, Lu et al. (2014) adopts a simplified halo quenching model to mimic the effects of AGN feedback that stops radiative cooling in high-mass haloes. In this model, radiative cooling is randomly switched off when haloes reach a critical mass of 10^{12} $M_\odot$ (with a Gaussian spread of ∼0.3 dex). In Benson (2012), the GALACTICUS model is more sophisticated and follows the growth and spins of black holes. The AGN jet power is computed from the accretion rates and spins of the black hole and is used to counterbalance radiative cooling in the hot halo. The parameters of the GALACTICUS model are tuned to produce a transition around few 10^{12} $M_\odot$ in halo mass, such that quenching begins above that mass. In this sense, quenching will be stochastic at $M_{\rm halo} \gtrsim 10^{12}$ $M_\odot$ but also depends on the black hole accretion rate and spin. In the GALACTICUS model, feedback may also shut down temporarily, for example after a merging event with high accretion rates which causes the black hole accretion disc to transition to a thin (radiative) mode with weaker jet power.

It is thus interesting to ask what drives colour in massive galaxies which live in haloes above 10^{12} $M_\odot$. Is colour a stochastic processes that is simply linked to small episodic amounts of gas cooling and/or merging events? Or is the colour in massive galaxies linked to halo properties such as halo age and hence perhaps more fundamentally tied to the large scale reservoir of fuel and the assembly history?

Our current paper does not fully account for the colour selection of CMASS but we can address some of the questions above. In our AbM model, galaxy colour is randomly assigned at fixed stellar mass. In the AgM model, on the other hand, colour is correlated with $z_{\rm starve}$ and hence with subhalo age. The degree to which colour correlates with $z_{\rm starve}$ is left as a free parameter and determined from the data. We have shown that both models can reproduce the galaxy SMF as well as $w_{\rm p}$ but fail to match the pseudo-multipoles.

To begin, let us focus on the consequences of Fig. 12 in terms of the AbM model. Because the mean stellar mass of the CMASS sample increases with redshift, the AbM model predicts a strong variation in the clustering amplitude with redshift which is clearly ruled out by the data. Hence, we argue that *the stochastic colour model (i.e. the AbM model) can be ruled out with high significance by our analysis.*

We now turn our attention to the AgM model. Our current implementation of the AgM model provides an excellent description of the SMF and w_p but fails to reproduce the pseudo-multipoles. However, unlike in the case of the AbM model in which the redshift dependence of the colour cuts are unimportant, we *know* that our AgM model will be sensitive to these effects which we have treated in a simplistic fashion. In a forthcoming paper, we will investigate if a more realistic AgM model which accounts for the colour completeness of CMASS with redshift can describe the redshift dependent multipoles. This approach should provide with powerful constraints on the physical mechanism that drives galaxy colour in massive haloes.

8 SUMMARY AND CONCLUSIONS

The last decade has seen rapid observational progress in our understanding of the relationship between galaxies and their underlying dark matter haloes, However, the connection between galaxies and dark matter remains poorly constrained for massive galaxies with $\log_{10} M_* \gtrsim 11.5$ because these galaxies are rare with low number densities, and require large areas surveys to obtain statistically significant samples. The BOSS survey provides a spectroscopic data set of massive galaxies at intermediate redshifts with number densities of $\bar{n} \approx 3 \times 10^{-4}$ $[(h^{-1}\,{\rm Mpc})^{-3}]$ in a survey volume that covers several cubic Gigaparsec (the 'CMASS' sample). This gigantic data set enables high-signal-to-noise ratio measurements of three dimensional galaxy clustering of massive galaxies.

In this paper, we introduce a novel method based on the SHAM framework that can be used to model complex populations such as CMASS by accounting for stellar mass (and eventually colour) completeness as a function of redshift. CMASS is referred to as a 'constant stellar mass' sample but L16 demonstrate that CMASS is only truly stellar mass limited in a narrow mass and redshift range. In order to fully utilize this sample to understand the galaxy-halo connection, it is critical to account for the CMASS mass completeness function. Our paper accounts for these effects and hence addresses an important limitation of the CMASS sample which has typically been neglected in previous work. Our mock catalogues account for CMASS selection effects, reproduce the overall SMF, the two-point correlation function of CMASS, and the CMASS dn/dz; the HOD table as a function of redshift; all made publicly available at www.massivegalaxies.com. After submitting our paper, a related effort by Rodríguez-Torres et al. (2016) was brought to our attention. Several key differences between Rodríguez-Torres et al. (2016) and our work include the choice of the input SMF, as well as the methodology for introducing scatter between stellar and halo mass.

We use data from Stripe 82 to measure the total SMF down to $\log_{10} M_* \gtrsim 11.5$ and perform a joint fit to both the SMF and the projected two point correlation function of CMASS galaxies. Our SHAM model (our 'AbM model') provides an excellent description of these two observables. Previous work has assumed that the CMASS HOD does not evolve with redshift. We re-investigate this assumption and show that the CMASS HOD should in fact vary strongly with redshift. Our model predicts that both the mean halo mass and the CMASS satellite fraction should vary with redshift. This variation is driven by the fact that the mean stellar mass of the sample increases at higher redshifts. In conclusion, our work suggests that CMASS is a complex sample for which the HODs are likely to vary with redshift in a non-trivial manner.

The colour selection applied to the CMASS sample may cause the two-point correlation function to be sensitive to assembly bias effects. We study the impact of such effects on the two-point correlation function using the age matching framework recently introduced

by H13. In contrast with H13, our sample lies firmly above collapse mass at $z \sim 0.55$, which corresponds to a relatively unexplored mass range. We demonstrate that in this regime, the effects of assembly bias are markedly different compared to the ones explored by H13 at lower stellar masses. For example, unlike H13, in this regime $z_{\rm starve}$ is dominated by $z_{\rm char}$ and not by $z_{\rm form}$. Also, the $z_{\rm form}$ component of $z_{\rm starve}$ causes red galaxies to cluster *less* strongly than blue ones. However, we also find that the rank ordering according to $z_{\rm starve}$ produces the opposite effect and causes an *increase* in the clustering amplitude. We show that an excellent fit to the CMASS two-point correlation function (which includes assembly bias effects) can be achieved by balancing these two opposing effects.

Overall, our two distinct models (standard abundance matching and age matching) can reproduce the galaxy SMF as well as $w_{\rm p}$, suggesting at first view a fundamental degeneracy between these models. However, we show that *both models fail to reproduce the pseudo multipoles* even though both models provide a satisfactory description of $w_{\rm p}$. Hence, our paper provides a clear cautionary example of the limitation of inferring the galaxy-halo connection from the projected correlation function alone.

We investigate the redshift dependent clustering of CMASS and find that the observed stellar mass variation of the CMASS sample should lead to more than a factor of 2.0 increase in the clustering amplitude over the CMASS redshift range which is in stark contrast with the data. We argue that this discrepancy suggests that, in addition to stellar mass, galaxy colour must also play an important role in determining the clustering amplitude of CMASS galaxies and that the observed constant clustering of CMASS may be due to a coincidental compensation between colour and stellar mass with redshift. Given a discrepancy in shape of the multipole correlation function, it may be necessary to consider velocity bias as recently studied in R14 and Guo et al. (2014) in the HOD framework. However, the velocity bias between subhaloes and galaxies are not well investigated yet for the mass scale and redshift range of our interest, and we defer this aspect to future work (but see Guo et al. (2016) for such an effort against the SDSS main sample).

Finally, we discuss the physical processes that drive galaxy colour in high-mass haloes. We are interested in determining if colour in these massive galaxies is a stochastic processes that is simply linked to small episodic amounts of gas cooling and/or merging events. Or is colour in massive galaxies linked to halo properties such as halo age and hence perhaps more fundamentally tied to the large scale reservoir of fuel and the assembly history? The stochastic scenario corresponds to our AbM model in which galaxy colour is randomly assigned at fixed stellar mass. Because the comparison of the redshift dependent clustering of CMASS with our AbM model, we argue that the stochastic colour model can be ruled out with high significance by our analysis. In this case, colour in high-mass haloes may be linked to other properties besides halo peak velocity, suggesting that assembly bias effects may play a role in determining the clustering properties of this sample.

Our current implementation of age-matching also fails to reproduce the pseudo-multipoles. However, unlike in the case of the AbM model in which redshift dependence of the colour cuts are unimportant, we *know* that our AgM model will be sensitive to these effects which we have treated in a simplistic fashion. Hence, in a forthcoming paper, we will characterize the CMASS colour distributions in greater detail and investigate if a more realistic age-matching model can describe the CMASS pseudo-multipoles. This approach will provide powerful constraints on the physical mechanisms that drives galaxy colour in massive haloes.

ACKNOWLEDGEMENTS

We are grateful to Francisco Prada, Risa Wechsler, Chiaki Hikage, and Surhud More for useful discussions. We acknowledge Yu Lu and Andrew Benson for useful discussions related to SAMs. This work was supported by World Premier International Research Center Initiative (WPI Initiative), MEXT, Japan. Numerical computations were partly carried out on Cray XC30 at Center for Computational Astrophysics, National Astronomical Observatory of Japan. SS is supported by a Grant-in-Aid for Young Scientists (Start-up) from the Japan Society for the Promotion of Science (JSPS) (No. 25887012). The MultiDark Database used in this paper and the web application providing online access to it were constructed as part of the activities of the German Astrophysical Virtual Observatory as result of a collaboration between the Leibniz-Institute for Astrophysics Potsdam (AIP) and the Spanish MultiDark Consolider Project CSD2009-00064. The Bolshoi and MultiDark simulations were run on the NASA's Pleiades supercomputer at the NASA Ames Research Center. The MultiDark-Planck (MDPL) and the BigMD simulation suite have been performed in the Supermuc supercomputer at LRZ using time granted by PRACE. Funding for SDSS-III has been provided by the Alfred P. Sloan Foundation, the Participating Institutions, the National Science Foundation, and the U.S. Department of Energy Office of Science. The SDSS-III web site is http://www.sdss3.org/. SDSS-III is managed by the Astrophysical Research Consortium for the Participating Institutions of the SDSS-III Collaboration including the University of Arizona, the Brazilian Participation Group, Brookhaven National Laboratory, Carnegie Mellon University, University of Florida, the French Participation Group, the German Participation Group, Harvard University, the Instituto de Astrofisica de Canarias, the Michigan State/Notre Dame/JINA Participation Group, Johns Hopkins University, Lawrence Berkeley National Laboratory, Max Planck Institute for Astrophysics, Max Planck Institute for Extraterrestrial Physics, New Mexico State University, New York University, Ohio State University, Pennsylvania State University, University of Portsmouth, Princeton University, the Spanish Participation Group, University of Tokyo, University of Utah, Vanderbilt University, University of Virginia, University of Washington, and Yale University.

REFERENCES

Ahn C. P. et al., 2014, ApJS, 211, 17
Aihara H. et al., 2011, ApJS, 193, 29
Alam S. et al., 2015, ApJ, 219, 12
Anderson L. et al., 2014, MNRAS, 441, 24
Baldry I. K., Glazebrook K., Driver S. P., 2008, MNRAS, 388, 945
Behroozi P. S., Conroy C., Wechsler R. H., 2010, ApJ, 717, 379
Behroozi P. S., Wechsler R. H., Wu H.-Y., 2013a, ApJ, 762, 109
Behroozi P. S., Wechsler R. H., Wu H.-Y., Busha M. T., Klypin A. A., Primack J. R., 2013b, ApJ, 763, 18
Benson A. J., 2012, New Astron., 17, 175
Berlind A. A., Weinberg D. H., 2002, ApJ, 575, 587
Beutler F. et al., 2014a, MNRAS, 443, 1065
Beutler F. et al., 2014b, MNRAS, 444, 3501
Bolton A. S. et al., 2012, AJ, 144, 144
Bundy K. et al., 2010, ApJ, 719, 1969
Bundy K. et al., 2015, ApJS, 221, 15
Carlson J., White M., 2010, ApJS, 190, 311
Chabrier G., 2003, PASP, 115, 763
Coil A. L. et al., 2011, ApJ, 741, 8
Conroy C., Wechsler R. H., Kravtsov A. V., 2006, ApJ, 647, 201
Coupon J. et al., 2015, MNRAS, 449, 1352
Croton D. J. et al., 2006, MNRAS, 365, 11

Dalal N., White M., Bond J. R., Shirokov A., 2008, ApJ, 687, 12
Davis M., Peebles P. J. E., 1983, ApJ, 267, L465
Dawson K. S. et al., 2013, AJ, 145, 10
Dekel A., Birnboim Y., 2006, MNRAS, 368, 2
Eisenstein D. J. et al., 2011, AJ, 142, 72
Fèvre O. L. et al., 2015, A&A, 576, A79
Fraser-McKelvie A., Brown M. J. I., Pimbblet K. A., 2014, MNRAS, 444, L63
Fukugita M., Ichikawa T., Gunn J. E., Doi M., Shimasaku K., Schneider D. P., 1996, AJ, 111, 1748
Gao L., White S. D. M., 2007, MNRAS, 377, L5
Gao L., Springel V., White S. D. M., 2005, MNRAS, 363, L66
Gunn J. E. et al., 1998, AJ, 116, 3040
Gunn J. E. et al., 2006, AJ, 131, 2332
Guo H. et al., 2013, ApJ, 767, 122
Guo H. et al., 2014, MNRAS, 446, 578
Guo H. et al., 2016, MNRAS, 459, 3040
Guzzo L. et al., 2014, A&A, 566, A108
Hartlap J., Simon P., Schneider P., 2007, A&A, 464, 399
Hearin A. P., Zentner A. R., Berlind A. A., Newman J. A., 2013, MNRAS, 433, 659 (H13)
Hearin A. P., Watson D. F., van den Bosch F. C., 2015, MNRAS, 452, 1958
Hearin A. P., Watson D. F., Becker M. R., Reyes R., Berlind A. A., Zentner A. R., 2014, MNRAS, 444, 729
Ishiyama T., Enoki M., Kobayashi M. A. R., Makiya R., Nagashima M., Oogi T., 2015, PASJ, 67, 6116
Jing Y. P., Suto Y., Mo H. J., 2007, ApJ, 657, 664
Kitaura F.-S., Yepes G., Prada F., 2013, MNRAS, 439, L21
Knebe A. et al., 2011, MNRAS, 415, 2293
Komatsu E. et al., 2009, ApJS, 180, 330
Kravtsov A. V., Berlind A. A., Wechsler R. H., Klypin A. A., Gottlober S., Allgood B., Primack J. R., 2004, ApJ, 609, 35
Landy S. D., Szalay A. S., 1993, ApJ, 412, L64
Lawrence A. et al., 2007, MNRAS, 379, 1599
Leauthaud A. et al., 2011, ApJ, 744, 159
Leauthaud A. et al., 2016, MNRAS, 457, 4021 (L16)
Lewis A., Bridle S., 2002, Phys. Rev. D, 66, 103511
Li Y., Mo H. J., Gao L., 2008, MNRAS, 389, 1419
Lilly S. J. et al., 2007, ApJS, 172, 70
Lim S. H., Mo H. J., Wang H., Yang X., 2016, MNRAS, 455, 499
Lin Y.-T., Mandelbaum R., Huang Y.-H., Huang H.-J., Dalal N., Diemer B., Jian H.-Y., Kravtsov A., 2016, ApJ, 819, 119
Liu F. S., Mao S., Meng X. M., 2012, MNRAS, 423, 422
Lu Y. et al., 2014, ApJ, 795, 123
McDonald M. et al., 2012, Nature, 488, 349
Mandelbaum R., Seljak U., Kauffmann G., Hirata C. M., Brinkmann J., 2006, MNRAS, 368, 715
Mandelbaum R., Wang W., Zu Y., White S., Henriques B., More S., 2016, MNRAS, 457, 3200
Manera M. et al., 2012, MNRAS, 428, 1036
Maraston C., Strömbäck G., Thomas D., Wake D. A., Nichol R. C., 2009, MNRAS, 394, L107
Masaki S., Lin Y.-T., Yoshida N., 2013, MNRAS, 436, 2286
Masters K. L. et al., 2011, MNRAS, 418, 1055
Miyatake H. et al., 2015, ApJ, 806, 1
Miyatake H., More S., Takada M., Spergel D. N., Mandelbaum R., Rykoff E. S., Rozo E., 2016, Phys. Rev. Lett., 116, 041301
Mo H., van den Bosch F. C., White S., 2010, Galaxy Formation and Evolution. Cambridge Univ. Press, Cambridge
Montero-Dorta A. D. et al., 2014, preprint (arXiv:1410.5854)
More S., 2013, ApJ, 777, L26
More S., Miyatake H., Mandelbaum R., Takada M., Spergel D., Brownstein J., Schneider D. P., 2015, ApJ, 806, 17
Moster B. P., Somerville R. S., Maulbetsch C., van den Bosch F. C., Macciò A. V., Naab T., Oser L., 2010, ApJ, 710, 903
Moustakas J. et al., 2013, ApJ, 767, 50
Newman J. A. et al., 2013, ApJS, 208, 5
Nuza S. E. et al., 2013, MNRAS, 432, 743
Oke J. B., Gunn J. E., 1983, ApJ, 266, 713
Onions J. et al., 2012, MNRAS, 423, 1200
Prada F., Klypin A. A., Cuesta A. J., Betancort-Rijo J. E., Primack J., 2012, MNRAS, 423, 3018
Reddick R. M., Wechsler R. H., Tinker J. L., Behroozi P. S., 2013, ApJ, 771, 30
Reid B. A., Seo H.-J., Leauthaud A., Tinker J. L., White M., 2014, MNRAS, 444, 476 (R14)
Reid B. et al., 2016, MNRAS, 455, 1553
Riebe K. et al., 2013, Astron. Nachr., 334, 691
Rodríguez-Torres S. A. et al., 2016, in press
Ross A. J. et al., 2013, MNRAS, 437, 1109
Saito S., Takada M., Taruya A., 2011, Phys. Rev. D, 83, 043529
Saito S., Baldauf T., Vlah Z., Seljak U., Okumura T., McDonald P., 2014, Phys. Rev. D, 90, 123522
Samushia L. et al., 2014, MNRAS, 439, 3504
Schlegel D. J., Finkbeiner D. P., Davis M., 1998, ApJ, 500, 525
Skillman S. W., Warren M. S., Turk M. J., Wechsler R. H., Holz D. E., Sutter P. M., 2014, preprint (arXiv:1407.2600)
Smee S. A. et al., 2013, AJ, 146, 32
Smith R. E., 2012, MNRAS, 426, 531
Tinker J. L. et al., 2011, ApJ, 745, 16
Tinker J. L., George M. R., Leauthaud A., Bundy K., Finoguenov A., Massey R., Rhodes J., Wechsler R. H., 2012, ApJ, 755, L5
Tinker J. L., Leauthaud A., Bundy K., George M. R., Behroozi P., Massey R., Rhodes J., Wechsler R. H., 2013, ApJ, 778, 93
Tojeiro R. et al., 2014, MNRAS, 440, 2222
Vale A., Ostriker J. P., 2004, MNRAS, 353, 189
van den Bosch F. C., More S., Cacciato M., Mo H., Yang X., 2013, MNRAS, 430, 725
Watson D. F. et al., 2014, MNRAS, 446, 651
Wechsler R. H., Zentner A. R., Bullock J. S., Kravtsov A. V., Allgood B., 2006, ApJ, 652, 71
White M. et al., 2011, ApJ, 728, 126
White M., Tinker J. L., McBride C. K., 2013, MNRAS, 437, 2594
Zehavi I. et al., 2005, ApJ, 630, 1
Zehavi I. et al., 2011, ApJ, 736, 59
Zentner A. R., Hearin A. P., van den Bosch F. C., 2014, MNRAS, 443, 3044
Zhao G.-B. et al., 2013, MNRAS, 436, 2038
Zheng Z. et al., 2005, ApJ, 633, 791
Zu Y., Mandelbaum R., 2016, MNRAS, 457, 4360

APPENDIX A: TESTS OF THE SUBHALO CATALOGUE

In this appendix, we discuss potential issues in the subhalo catalogue, focusing in particular on the time evolution of subhalo clustering and completeness issues due to the resolution of the simulation.

We begin by testing if a single redshift output is sufficient to model CMASS over the redshift range of $0.43 < z < 0.7$. We rank order subhaloes by $V_{\rm peak}$ and select the top N subhaloes with a number density of $\overline{n} \simeq 1.58 \times 10^{-4} (h^{-1}\,{\rm Mpc})^{-3}$. This value roughly corresponds to the number density of galaxies with $\log_{10}(M_*/{\rm M}_\odot) \gtrsim 11.0$. Fig. A1 shows the three-dimensional correlation function of subhaloes in real space as a function of separation at three different redshift outputs and at fixed number density $\overline{n}$. The correlation function varies by at most 5 per cent compared to $z = 0.534$ over the CMASS redshift range. The fractional difference at large scales, $r \gtrsim 3\,h^{-1}$ Mpc, is 1–2 per cent. The largest differences (at the level of 5 per cent) are seen at the transition regime from the 2-halo to 1-halo term, $r \lesssim 1\,h^{-1}$ Mpc, where the errors on our observational clustering signal are increased by uncertainties due to the fibre-collision correction. In future work, especially when the

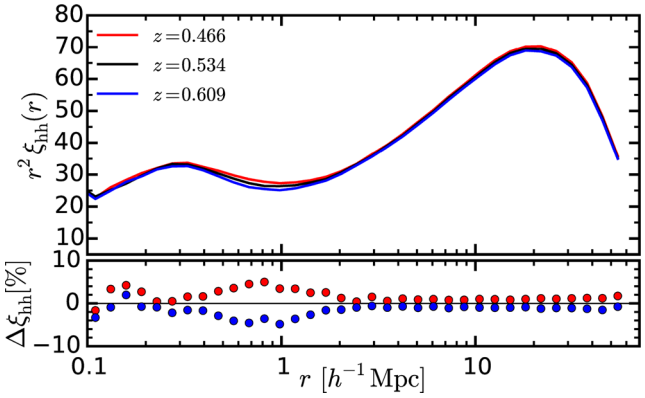

Figure A1. Time evolution of the clustering of subhaloes at fixed number density. Subhaloes are inversely sorted by $V_{\rm peak}$ and a cut is imposed at a number density of $\bar{n} \simeq 1.58 \times 10^{-4}(h/{\rm Mpc})^3$. The upper panel shows a comparison of the three dimensional correlation function of subhaloes in real space at different redshift outputs; $z = 0.436$ (red), $z = 0.534$ (default, black), and $z = 0.609$ (blue). The lower panel presents a fractional difference of the correlation function with respect to the one at the default $z = 0.534$ output.

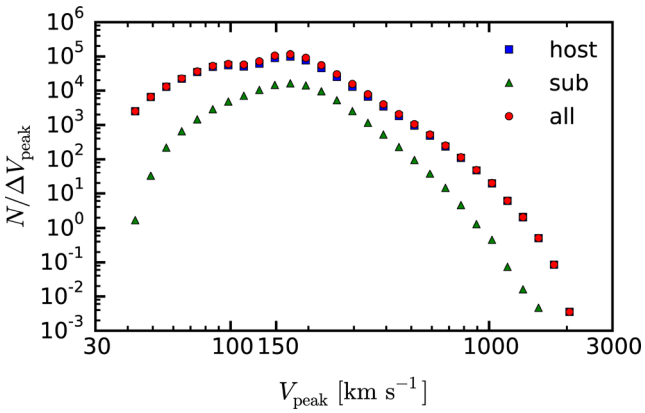

Figure A2. The histogram of host haloes (blue square), subhaloes (green triangle), and all haloes (red circle) as a function of $V_{\rm peak}$. A clear turnover around $V_{\rm peak} \sim 150\,{\rm km\,s^{-1}}$ suggests that subhaloes with $V_{\rm peak} \gtrsim 150\,{\rm km\,s^{-1}}$ are not affected by resolution.

S/N of the measurements increase (currently we are using DR10 measurements), these effects will need to be taken into account.

We perform two tests concerning the impact of the resolution of MDR1 on our results. Based on White et al. (2011) and also R14, we estimate that abundance matching for CMASS will require subhaloes with $V_{\rm peak} \geq 200\,{\rm km\,s^{-1}}$. Fig. A2 presents the histogram of subhaloes as a function of $V_{\rm peak}$. This histogram starts to deviate from a power law at $V_{\rm peak} \sim 200\,{\rm km\,s^{-1}}$ and has a clear turnover at $V_{\rm peak} \sim 150\,{\rm km\,s^{-1}}$. Fig. A2 demonstrates that MDR1 has a sufficient resolution for CMASS, although a higher resolution would be preferable.

However, Fig. A2 does not guarantee that the resolution is sufficiently high to trust our clustering predictions down to arbitrarily small scales. Our clustering signal is dominated by central-satellite pairs in the 1-halo term regime, implying that it is important to study the completeness of subhaloes as a function of distance to their host–hosts, $R_{\rm sub}$. Because the true radial profiles of subhaloes remain poorly known, it is difficult to precisely characterize the radius at which incompleteness effects become important. With this caveat in mind, Behroozi et al. (2013b) define the radius at which

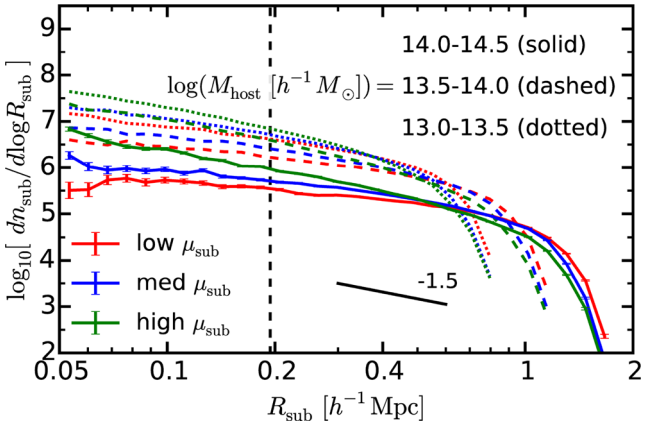

Figure A3. Radial profiles of subhaloes. Different colours correspond to different values of $\mu_{\rm sub} \equiv V_{\rm peak}^{\rm sub}/V_{\rm peak}^{\rm host}$. The samples in terms of $\mu_{\rm sub}$ are created to contain an equal number of subhaloes. The solid, dashed, and dotted lines correspond to three different bins in host halo mass (but divided in terms of $V_{\rm peak}$). As a reference, the logarithmic slope of -1.5 is also shown. The radius at which subhalo detections are incomplete is estimated as the radius where the logarithmic slope of the profile becomes larger than -1.5. The vertical black dashed line shows the minimum scale in our clustering measurement.

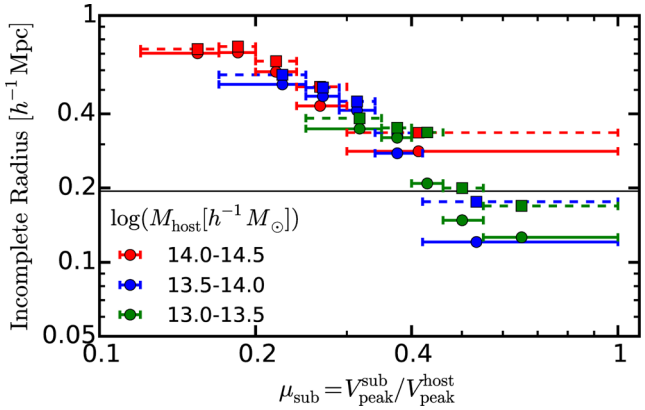

Figure A4. Subhalo incompleteness radius as a function of $\mu_{\rm sub}$. Different colours indicate different bins in host halo mass. Circles with solid error bars show the results when the incomplete radius is defined with respect to a logarithmic slope of -1.5. Squares with dashed error bars represent the results when the incomplete radius is defined with respect to a logarithmic slope of -1.7. The horizontal black dashed line shows the minimum scale in our clustering measurement. Higher resolution simulations would be preferable and will be adopted in forthcoming paper.

subhalo detections are incomplete as the radius where the logarithmic slope of the profile becomes larger than -1.5 (or -1.7). This cut-off is motivated by the density profiles of observed subhaloes in the maxBCG cluster catalogue (Tinker et al. 2011). Fig. A3 displays the radial profiles of subhaloes for different ratios of $V_{\rm peak}$, $\mu_{\rm sub} \equiv V_{\rm peak}^{\rm sub}/V_{\rm peak}^{\rm host}$, and for three different bins in host halo mass (but divided by $V_{\rm peak}$). In general, this radial profile becomes gradually shallower at smaller $R_{\rm sub}$ due to the fact that density contrast between the parent halo and subhaloes decreases in the inner regions of haloes and subhaloes become more difficult to detect. Using the Behroozi et al. (2013b) criterion, we estimate that subhalo detections become incomplete at 0.1–0.7 h^{-1} Mpc, depending on $\mu_{\rm sub}$ and $M_{\rm host}$, as shown in Fig. A4. The smallest scale in our w_p measurement is $\approx 0.2\,h^{-1}$ Mpc and is indeed close to the

incompleteness limit. We can definitely improve this situation by using higher resolution simulations. However, we expect that the impact of the resolution on our results should be relatively small, since the errors of our measured w_p on these scales are boosted by systematic uncertainties in the fibre collision correction. We conclude that the resolution of MDR1 is sufficient for our purpose, but higher resolution simulations would be preferable and will be adopted in subsequent work.

APPENDIX B: IMPACT OF THE SCATTER IN THE $V_{\rm peak} - M_*$ RELATION FOR THE AGE-MATCHING MODEL

To study the impact of the assembly bias effect, we adopt the age-matching model where we reorganize the relation between subhalo age and galaxy colour at fixed stellar mass rather than at fixed halo mass (or $V_{\rm peak}$). This is because we can perform rank-order matching only against observable quantities. However, because our study operates in the very steep end of the SMF, we must verify that our results do not depend on the stellar mass bin width when performing age-matching. In H13, the authors report that their analysis is insensitive to a stellar-mass bin width of $\Delta \log M_* = 0.05$–0.2. In this appendix, we perform a similar exercise to H13 for our extreme age-matching model (see Section 6.3). In the following, we demonstrate that our results are insensitive to our fiducial bin width of $\Delta \log M_* = 0.05$. However, we also show that the choice of a fiducial bin width needs to take into consideration the scatter (in our case $\sigma = 0.105$).

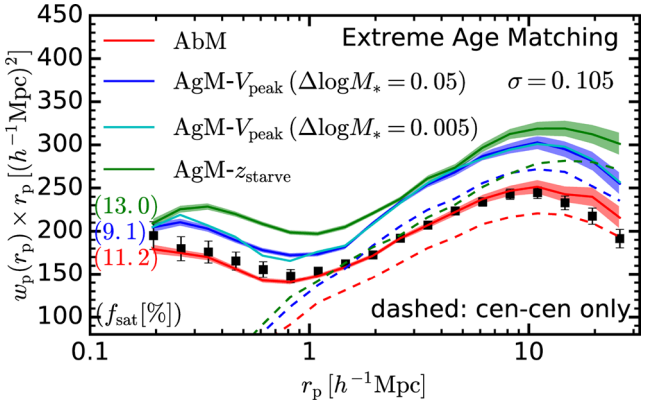

Figure B1. Testing our stellar-mass bin width in performing the age-matching model. We perform the age-matching model for the extreme case as discussed in Section 6.3 but in terms of $V_{\rm peak}$ itself as a halo-age proxy. Note that the best-fitting values in the simple age matching, (ϕ_1, $\log_{10}M_0$, σ) = (1.86×10^{-3}, 10.89, 0.105), are adopted here. $w_{\rm p}$ with the different bin size are shown in blue for $\Delta \log M_* = 0.05$ and in cyan for 0.005, respectively. These results can be compared with the age-matching one (red) where a clear discrepancy with blue or cyan curve is confirmed. The age-matching model with $z_{\rm starve}$ is also shown just for a comparison with Fig. 7.

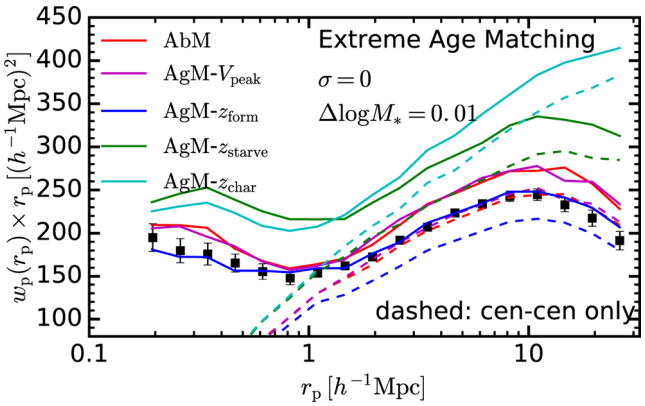

Figure B2. Testing the impact of the scatter in the $V_{\rm peak} - M_*$ relation on the age-matching model. Here we fix the bin width with $\Delta \log M_* = 0.01$ and do not introduce the scatter, i.e. $\sigma = 0$. In this case, the abundance matching (red) and the age matching with $V_{\rm peak}$ (magenta) result in identical clustering. As a comparison, the age-matching results with $z_{\rm form}$ (blue), $z_{\rm starve}$ (green), and $z_{\rm char}$ (cyan) are also plotted to manifest the pure assembly bias effect in absence of the scatter.

We perform a test in which we consider the extreme age-matching model in Section 6.3 but we reshuffle with respect to $V_{\rm peak}$ rather than $z_{\rm starve}$. In addition, we test how the results vary if we use a different bin width. Fig. B1 demonstrates that our results are insensitive to this change in bin width ($\Delta \log M_* = 0.05$ (blue) and $\Delta \log M_* = 0.005$ (cyan)). We have also checked that our mean halo masses and satellite fractions are unchanged when going from $\Delta \log M_* = 0.05$ to $\Delta \log M_* = 0.005$.

Nevertheless, Fig. B1 shows a clear difference between the simple abundance matching ('AbM', red) and the extreme age matching results ('AgM-$V_{\rm peak}$', blue or cyan). In fact, the mean halo mass and the satellite fraction for the AbM (AgM-$V_{\rm peak}$) models are $\log(\overline{M_{\rm vir}}\,[{\rm M}_\odot h^{-1}]) = 13.442$ (13.551), and $f_{\rm sat} = 11.08$ per cent (9.12 per cent), respectively. We argue that this difference originates from the non-zero scatter in the $V_{\rm peak} - M_*$ relation in the abundance matching. In performing the extreme age-matching model with $V_{\rm peak}$, CMASS galaxies with larger $X_{\rm col}$ at fixed stellar mass are likely to have larger $V_{\rm peak}$.

Our argument is confirmed by Fig. B2 where we perform the same exercise but we set $\sigma = 0$. In this case, we find that our clustering prediction becomes stable with bin widths smaller than $\Delta \log M_* = 0.01$, and that AbM result is similar to the AgM-$V_{\rm peak}$ one (compare red with magenta lines). In Fig. B2, we also display the AgM model with a variety of halo-age indicators (see Section 6.3). The haloes masses of the blue, green and cyan curves are very similar ($\log(\overline{M_{\rm vir}}\,[{\rm M}_\odot h^{-1}]) = 13.513$). Hence, differences in the clustering for the blue, green and cyan curves are a consequence of assembly bias effects.

This paper has been typeset from a TEX/LATEX file prepared by the author.